COMMUNICATIONS

DE LA FACULTE DES SCIENCES
DE L'UNIVERSITE D'ANKARA

FACULTY OF SCIENCES
ANKARA UNIVERSITY

Series A2-A3: Physical Sciences and Engineering

VOLUME: 60 **Number: 1** **YEAR: 2018**

Faculy of Sciences, Ankara University
06100 Beşevler, Ankara-Turkey
ISSN 1303-6009 e-ISSN 2618-6462

COMMUNICATIONS

DE LA FACULTE DES SCIENCES
DE L'UNIVERSITE D'ANKARA

FACULTY OF SCIENCES
ANKARA UNIVERSITY

Series A2-A3: Physical Sciences and Engineering

This Journal is published two issues in a year by the Faculty of Sciences, Ankara University. Articles and any other material published in this journal represent the opinions of the author(s) and should not be construed to reflect the opinions of the Editor(s) and the Publisher(s).

Correspondence Address:
COMMUNICATIONS
EDITORIAL OFFICE
Ankara University, Faculty of Sciences
06100 Tandogan, ANKARA – TURKEY
Tel: (90) 312-212 6720 Fax: (90) 312-223 5000
e-mail: commun@science.ankara.edu.tr
http://communications.science.ankara.edu.tr/index.php?series=A2A3

Print:
Ankara University Press
Tandogan Campus 06100
ANKARA – TURKEY
Tel: (90) 312-215 9001

COMMUNICATIONS

DE LA FACULTE DES SCIENCES
DE L'UNIVERSITE D'ANKARA

FACULTY OF SCIENCES
ANKARA UNIVERSITY

VOLUME: 60 **Number: 1** **YEAR: 2018**

Series A2-A3: Physical Sciences and Engineering

COMMUNICATIONS

DE LA FACULTE DES SCIENCES
DE L'UNIVERSITE D'ANKARA

FACULTY OF SCIENCES
ANKARA UNIVERSITY

VOLUME: 60 **Number: 1** **YEAR: 2018**

Series A2-A3: Physical Sciences and Engineering

Commun.Fac.Sci.Univ.Ank.Series A2-A3
Volume 60, Number 1, Pages 1–10 (2018)
DOI: 10.1501/commua1-2_0000000106
ISSN 1303-6009 E-ISSN 2618-6462
http://communications.science.ankara.edu.tr/index.php?series=A2A3

ENTROPY EXCHANGE AND ENTANGLEMENT IN THE JAYNES-CUMMINGS MODEL WITH TRANSIENT EFFECTS

HÜNKAR KAYHAN

Abstract. In this paper, we investigate the dynamics of entropy exchange and entanglement in the atom-field interaction by the Jaynes-Cummings model in the presence of the transient effects considered for the case of linear sweep. We find that the transient effects do not influence the entropy exchange between the atom and the field. As the strength of these effects increases, the oscillations of the entropy change and entanglement speed up. The entanglement behaves chaotically as the transient effects become stronger

Introduction

Cavity Quantum Electrodynamics (CQE) keeps an important place in quantum optics and attracts much attention [1, 2, 3]. Perhaps, the simplest model of CQE is the Jaynes-Cummings Model (JCM) [4]. The model describes the system of a two-level atom interacting with a quantized mode of an optical cavity, with or without the presence of light. In spite of its simplicity, the JCM reveals important properties of light such as the discreteness of field states [1, 5]. The model is open to some extensions to consider additional effects. Some of the extensions are initial conditions [6], dissipation and damping [7, 8, 9], multilevel atoms and multiple atoms [10] and multi-mode description of the field [11]. Another extension of the JCM is incorporation of the transient effects considered for the linear sweep as studied by Joshi and Lawande [12]. Experimentally, this extension can describe an atom entering a cavity subjecting to a very slow shift or a sudden jump of the electric field. Linear sweep model was considered elsewhere [13, 14]. We previously studied the influence of the transient effects on the dynamics of entanglement between a JCM atom and an isolated atom [15]. We showed that the entanglement sudden death can be controlled by these transient effects. Transient effects has also been studied elsewhere [16, 17].

Received by the editors: September 05, 2017; Accepted: December 25, 2017.

PACS numbers. PACS numbers:42.50.Ct, 03.65.Ud.

Key words and phrases. entropy exchange, entanglement, transient effects, Jaynes-Cummings model.

Boukobza and Tannor [18] studied the JCM for the mixed states of field and atom and showed that there is an entropy exchange between the field and the atom. The entropy exchange dynamics in the atom-field interactions was studied extensively elsewhere [19, 20, 21, 22, 23, 24].

In this paper, we use the model in Ref. [12] to study the dynamical properties of entropy correlations and entanglement in the atom-field interaction in the presence of the transient effects. We show that the transient effects do not influence the dynamical behavior of entropy exchange between the atom and the field. As the strength of these effects increases, the oscillations of the entropy change and entanglement speed up. The entanglement behaves chaotically as the transient effects become stronger.

SYSTEM AND SOLUTION

The Hamiltonian of the system with the resonance between the atomic transition and the field frequencies is ($\hbar = 1$) [4]

$$H = \omega S_z + \omega a^\dagger a + g(S_+ a + S_- a^\dagger) \tag{1}$$

where $S_\pm$ and S_z are spin-1/2 atomic operators, a and $a^\dagger$ are the field annihilation and creation operators and also g is the coupling coefficient between the atom and the field. In order to incorporate the transient effects, the coupling coefficient g is modified as [12]

$$g(t) = g f(t) \tag{2}$$

where the function $f(t)$ describes the linear sweep. $f(t)$ contains the two limiting cases which correspond to sudden jump and adiabatic variation. The cavity-mode quantized field is switched on by a linear ramp described by this function. It is defined as

$$\begin{array}{rclll} f(t) & = & kt/T & for & 0 \leq t \leq T \\ & & 0 & otherwise & \end{array}$$

As the value of k increases over a fixed time interval T from small values to large values, the strength of the interaction changes from adiabatic variation to sudden jump.

The atom is initially taken in a mixed state

$$\rho^a(0) = P_e|e\rangle\langle e| + P_g|g\rangle\langle g| \tag{3}$$

with $P_e + P_g = 1$ and $0 \leq P_e, P_g \leq 1$ and the field is initially taken in a thermal state

$$\rho^f(0) = \sum_{n=0} P_n|n\rangle\langle n| \tag{4}$$

whose probability distribution P_n is given by

$$P_n = \frac{1}{(1+\langle n\rangle)}\left(\frac{\langle n\rangle}{1+\langle n\rangle}\right)^n \tag{5}$$

where $\langle n\rangle$ is the initial mean photon number in the cavity. So, the initial state of the total system which is a product state, becomes

$$\rho^{fa}(0)=\rho^{f}(0)\otimes\rho^{a}(0)=P_e\sum_{n=0}P_n|ne\rangle\langle ne|+P_g\sum_{n=0}P_n|ng\rangle\langle ng| \qquad (6)$$

where $|ne\rangle=|n\rangle\otimes|e\rangle$ and $|ng\rangle=|n\rangle\otimes|g\rangle$. The Hamiltonian operator of our system is time-dependent due to the coupling $g(t)$, but the Hamiltonians at different times commute. Then, time-evolution of the total system is obtained by

$$\rho^{fa}(t)=\exp[-i\int_0^t H(\acute{t})d\acute{t})]\rho^{fa}(0)\exp[i\int_0^t H(\acute{t})d\acute{t}] \qquad (7)$$

Then, we obtain

$$\begin{aligned}\rho^{fa}(t) \quad = \quad & P_e\sum_n P_n[\cos^2(c_{n+1}(t))|ne\rangle\langle ne|+i\sin(c_{n+1}(t))\cos(c_{n+1}(t))|ne\rangle\langle n+1g| \\ & -i\sin(c_{n+1}(t))\cos(c_{n+1}(t))|n+1g\rangle\langle ne|+\sin^2(c_{n+1}(t))|n+1g\rangle\langle n+1g|] \\ & +P_g\sum_n P_n[\cos^2(c_n(t))|ng\rangle\langle ng|+i\sin(c_n(t))\cos(c_n(t))|ng\rangle\langle n-1e| \\ & -i\sin(c_n(t))\cos(c_n(t))|n-1e\rangle\langle ng|+\sin^2(c_n(t))|n-1e\rangle\langle n-1e|] \qquad (8)\end{aligned}$$

where $c_n(t)=g\sqrt{n}\frac{kt^2}{2T}$. The density matrix of the atom (and the field) can be found by tracing out $\rho^{fa}(t)$ over the degree of freedom of the field (and the atom). The atomic density matrix becomes

$$\begin{aligned}\rho^{a}(t) \quad = \quad & \{P_e\sum_n P_n\cos^2(c_{n+1}(t))+P_g\sum_n P_{n+1}\sin^2(c_{n+1}(t))\}|e\rangle\langle e| \\ & +\{P_g\sum_n P_n\cos^2(c_n(t))+P_e\sum_n P_{n-1}\sin^2(c_n(t))\}|g\rangle\langle g| \qquad (9)\end{aligned}$$

The elements of the density matrix of the field becomes

$$\begin{aligned}\rho^{f}_{nn}(t) \quad = \quad & P_e\{P_n\cos^2(c_{n+1}(t))+P_{n-1}\sin^2(c_n(t))\}+ \\ & P_g\{P_n\cos^2(c_n(t))+P_{n+1}\sin^2(c_{n+1}(t))\} \qquad (10)\end{aligned}$$

RESULTS

We now numerically investigate the entropy correlations and the entanglement between the atom and the field by the figures. (In these, we assume that $g=1$.) For our computations, we truncate the series when $\sum_{n=0}P_n\approx 1$ [18]. For the entropy correlations, we compute the von-Neumann entropy of the atom and the field subsystems. The entropy of a system is defined as

$$S = -\sum_i \lambda_i \log \lambda_i \tag{11}$$

where λ_is are the non-zero eigenvalues of the relevant density matrix. The entropy change ($\Delta S = S(t) - S(0)$) for the atom and for the field can be computed by using their density matrices described in Eqs. (9) and (10).

Figs. (1)-(5) show the time-evolution of entropy changes of the atom and the field and their entanglement in the presence of the transient effects. Numerically, $k = 0.5$ may describe an adiabatic variation and $k = 8.0$ may describe a sudden jump in the interaction. As we move from the adiabatic variation case to the sudden jump case (the value of k increases), the periodic evolution of entropy changes and entanglement speeds up. In Fig. (1), the atom is in the excited state and the field is in a weakly excited thermal state with the average photon number $\langle n \rangle = 0.1$. The entropy changes of the atom and the field fluctuate together and so they are correlated. When the atom is taken to be in the ground state as shown in Fig. (2), the sum of the atom and field entropy changes is quasi-conserved. Their entropy relations are anti-correlated. There is an entropy exchange between the atom and the field, although the exchange is not complete. When the atomic state is close to ground state ($P_g = 0.9$), there is an almost complete entropy exchange, as shown in Fig. (3). The sum of the atom and field entropy changes is almost completely conserved. The transient effects do not have any influence on the behavior of the entropy exchange between the atomic and the field states. The sum of the entropy changes of the atom and the field is approximately zero in the presence of the transient effects.

For the entanglement properties of the system, we calculate a lower bound on concurrence (LBC) such that the joint state of the atom-field system $2 \otimes \infty$ is projected onto $2 \otimes 2$ systems by means of the projection operator

$$\Pi_n = (|g\rangle\langle g| + |e\rangle\langle e|) \otimes (|n\rangle\langle n| + |n+1\rangle\langle n+1|) \tag{12}$$

The resulting density operator is

$$\rho_n(t) = \frac{1}{T_n(t)} \Pi_n \rho^{fa}(t) \Pi_n \tag{13}$$

where $T_n(t) = \mathrm{Tr}(\Pi_n \rho^{fa}(t) \Pi_n)$ denotes the probability of obtaining $\rho_n(t)$ which is a sub-state with the dimension $2\otimes2$. For the $2\otimes2$ systems, the degree of entanglement can be quantified by the Wootters' concurrence [25]. Concurrence varies from 0 for the separable states to 1 for the maximally entangled states. Entanglement of the total system can be quantified by averaging over the entanglement of all the sub-states of the system [26]

$$C(t) = \frac{\sum_n T_n(t) C_n(t)}{\sum_n T_n(t)} \tag{14}$$

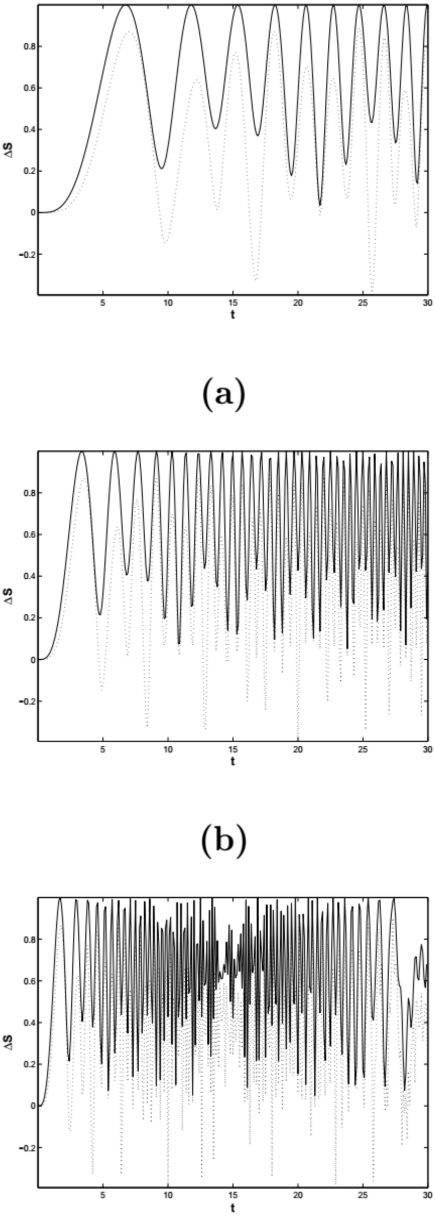

(a)

(b)

(c)

FIGURE 1. Entropy change ΔS for the atom (solid line) and for the field (dot line) as a function of time t. $P_e = 1$, $\langle n \rangle = 0.1$ and

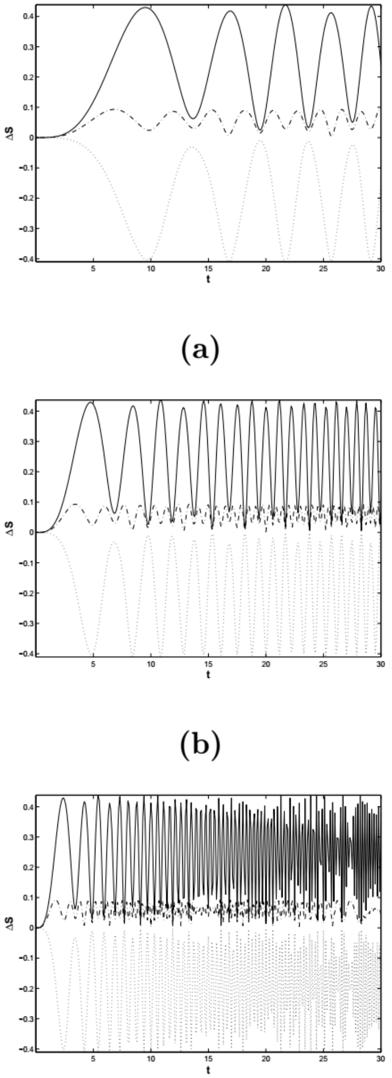

(a)

(b)

(c)

Figure 2. Entropy change ΔS for the atom (solid line), for the field (dot line) and for their sum (dash-dot line) as a function of time t. $P_g = 1$, $\langle n \rangle = 0.1$ and $T = 30$. **(a)** $k = 0.5$ **(b)** $k = 2.0$ **(c)** $k = 8.0$.

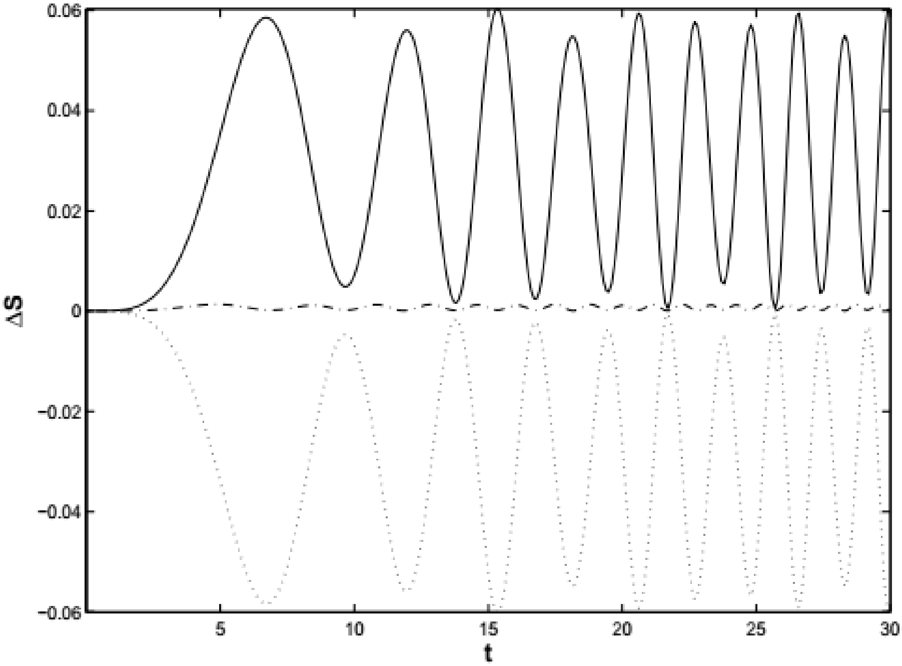

FIGURE 3. Entropy change ΔS for the atom (solid line), for the field (dot line) and for their sum (dash-dot line) as a function of time t. $P_g = 0.9$, $\langle n\rangle = 0.1$, $T = 30$ and $k = 1.0$.

where $C_n(t)$ is the concurrence of sub-state $\rho_n(t)$.

Fig. (4) shows the time-evolution of the entanglement of the system for $P_e = 1$. It is obvious that the time-elapsed for the collapse and recovery of the entanglement is long around the beginning of the interaction and then shortens, as time passes. Also, there is a time interval (around $t \approx 15$) at which the amplitude of the oscillations are relatively suppressed. So, there is some chaos at these instants of time in the interaction. We now calculate the time-average of the concurrence to see more clearly this chaotic influence of the transient effects on the entanglement. We compute it as

$$C_{av} = \frac{\int_0^T C(t)dt}{T} \tag{15}$$

where we take $T = 30$ and take the integral numerically.

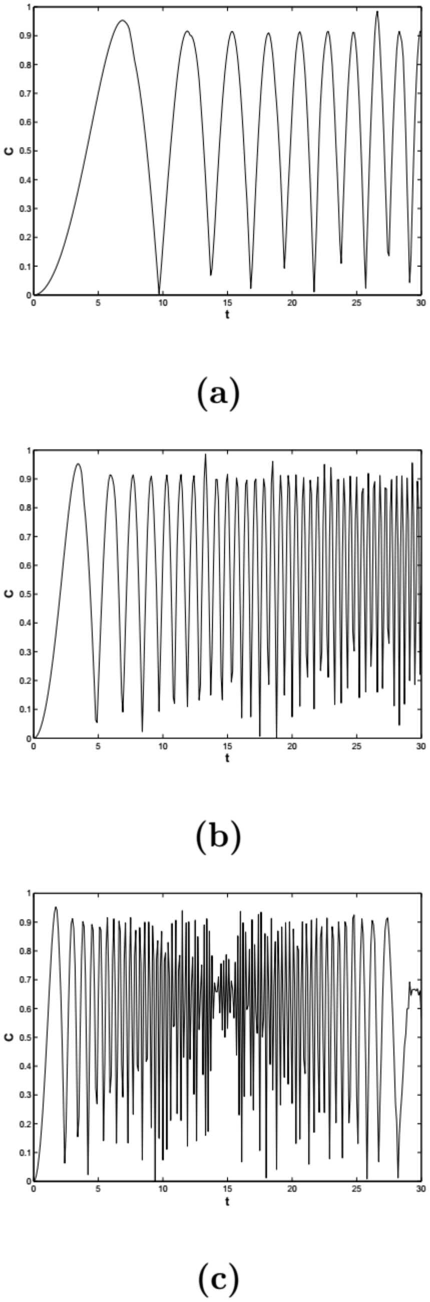

FIGURE 4. Concurrence C as a function of time t. $P_e = 1$, $\langle n \rangle = 0.1$ and $T = 30$. **(a)** $k = 0.5$ **(b)** $k = 2.0$ **(c)** $k = 8.0$.

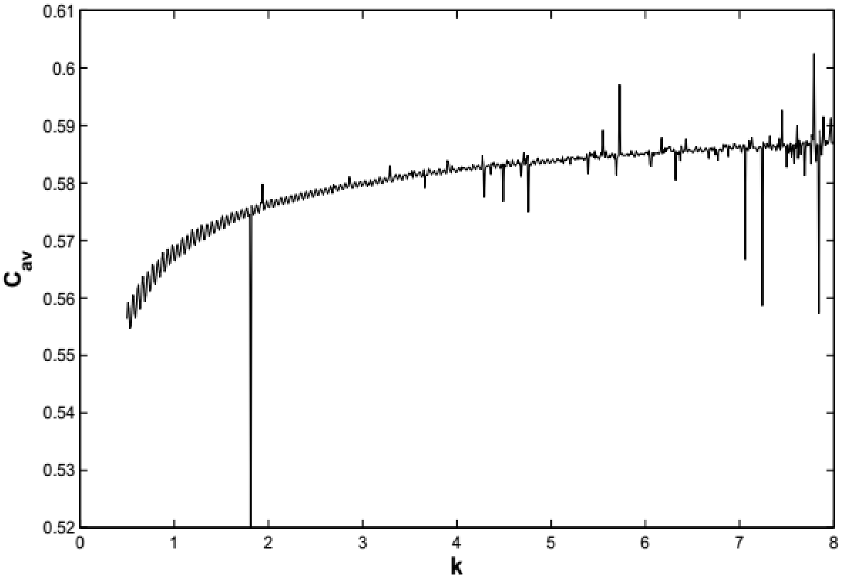

FIGURE 5. Average Concurrence C_{av} as a function of the parameter of the transient effects k. $P_e = 1$, $\langle n \rangle = 0.1$ and $T = 30$.

Fig. (5) shows the evolution of the time-averaged entanglement as a function the parameter of the transient effects. It is clear that the average entanglement fluctuates chaotically with the parameter k. There are unexpectedly considerable sharp rises and falls at some values of k. What we normally expect is the certain monotonic increase of the average entanglement with the parameter k. Apart from these random fluctuations, the higher values of k, the higher magnitude of the entanglement, as expected.

CONCLUSION

In summary, we have examined the dynamics of the entropy changes and the entanglement in the atom-field interaction by the Jaynes-Cummings model in the presence of the transient effects. We have showed that the transient effects do not influence the dynamical behavior of entropy exchange between the atom and the field. As the strength of these effects increases, the oscillations of the entropy change and entanglement speed up. The entanglement behaves chaotically as the transient effects become stronger.

ACKNOWLEDGEMENTS

I am grateful to the referees for their valuable comments and recommendations that improve this paper.

REFERENCES

[1] Eberly, J. H. , N. B. Narozhny, J. J. Sanchez-Mondragon, Phys. Rev. Lett. **44**, 1323 (1980).
[2] Wu, Y., X. X. Yang, Phys. Rev. Lett. **78**, 3086 (1997).
[3] İmamoğlu, A., S. E. Harris, Opt. Lett. **14**, 1344 (1989).
[4] Jaynes, E. T., F. W. Cummings, Proc. IEEE **51**, 89 (1962).
[5] Cummings, F. W., Phys. Rev. **140**, A1051 (1965).
[6] Kuklinski J. R. and J. L. Madajczyk, Phys. Rev. A **37**, 3175 (1988).
[7] Gea-Banacloche, J., Phys. Rev. A **47**, 2221 (1993).
[8] Rodriguez-Lara B. M. and H. Moya Cessa, Phys. Rev. A **71**, 023811 (2005).
[9] Kundu, A., Theor. Math. Phys **144**, 975 (2005).
[10] Hussin V. and L. M. Nieto, J. Math. Phys. **46**, 122102 (2005).
[11] Shore B. W., and P. L. Knight, J. Mod. Opt. **40**, 1195 (1993).
[12] Joshi, A., S. V. Lawande, Phys. Rev. A **48**, 2276 (1993).
[13] Agarwal G. S., and S. Arun Kumar, Phys. Rev. Lett. **67**, 3665 (1991).
[14] Graham, R., J. Mod. Opt. **34**, 873 (1987).
[15] Kayhan, H., Commun. Theor. Phys. **56**, 487 (2011).
[16] Hu Y.-H. and Y.-G. Tan, Phys. Scr. **89**, 075103 (2014).
[17] Hu Y.-H. and Y.-G. Tan, Commun. Theor. Phys. **62**, 49 (2014).
[18] Boukobza, E., D. J. Tannor, Phys. Rev. A **71**, 063821 (2005).
[19] Yan, X.-Q., B. Shao, J. Zou, Chaos, Solitons & Fractals **37**, 835 (2008).
[20] Zhang, J., B. Shao, J. Zou, Commun. Theor. Phys. **49**, 1463 (2008).
[21] Zhang, Y.-Q., L. Tan, Z.-H. Zhu, Z.-Z. Xiong, L.-W. Liu, Chin. Phys. B **19**, 024210 (2010).
[22] Guo, J.-L. Y.-B. Sun, Z.-D. Li, Opt. Commun. **284**, 896 (2011).
[23] Yan X.-Q. and Y.-G. Lü, Commun. Theor. Phys. **57**, 209 (2012).
[24] Yan, X.-Q., Chaos, Solitons & Fractals **45**, 1309 (2012).
[25] Wootters, W. K., Phys. Rev. Lett. **80**, 2245 (1998).
[26] Rendell R. W. and A. K. Rajagopal, Phys. Rev. A **67**, 062110 (2003).

Current address: Hünkar Kayhan: Department of Physics, Abant Izzet Baysal University, Bolu-14280, Turkey
E-mail address: `hunkar_k@ibu.edu.tr`
ORCID: `http://orcid.org/0000-0001-6340-8933`

Commun.Fac.Sci.Univ.Ank.Series A2-A3
Volume 60, Number 1, Pages 11-20(2018)
DOI: 10.1501/commua1-2_0000000107
ISSN 1303-6009 E-ISSN 2618-6462
http://communications.science.ankara.edu.tr/index.php?series=A2A3

COMMUNICATIONS
SERIES A2-A3

CRIME PREDICTION USING SOCIAL SENTIMENT AND SOCIO-FACTOR

SAKIRIN TAM AND Ö. ÖZGÜR TANRIÖVER

Abstract. Crime prediction becomes very important trend and a key technique in crime analysis to identify the optimal patrol strategy for police department. Many researchers have found number of techniques and solutions to analyze crime, using data mining techniques. These studies can help to speed up and computerize the process of crime analysis processes. However, the pattern of crime is flexible, it always changes and grows. With social media, user posts and discusses event publicly. These textual data of every user has contextual information of user's daily activities. These posts generate unstructured data that can be used for data prediction. As shown by previous research, twitter sentiment enable to predict crime in Chicago, United States. However, existed model on crime prediction was incorporating the use of socio factors. Therefore, the study aims to model crime prediction using social media content with additional socio-factors. The research approach is consisted of a combination of sentiment analysis from Twitter and social-factors with Kernel Density Estimation. Lexicon-base methods will be applied for sentiment analysis, and the model evaluation is measured with the help of logistic regression.

1. Introduction

Over the last decade, the exponential of social media development allows users to publish and access information and idea freely around the globe. With ease and effective use of social media, the number of Twitter users is grown from 140 million user with 340 million tweets or messages in 2012 [1] to 313 million users and 1 billion tweets or actively post on twitter [2]. Recent researches show that Twitter can be used for decision support as an ideal data source; users publicly discuss and distribute topics, emotions and events in real time with precise and valuable information called hashtag. Hashtag contains hidden information that can detect events and trend of topic [3]. As result, many researches used Twitter as predictive analytic data source to predict large-scale events in natural disaster [4], election [5] and crime [1] [6].

Received by the editors: November 11, 2017; Accepted: January 20, 2018.
Key word and phrases: Crime prediction, Data mining, Social media, Sentiment analysis, Socio-Factor.

Crime detection and prediction become very important trend and a key technique in crime analysis to identify the optimal patrol strategy for police department. Many researches have found number of techniques and solutions to analyze crime, using data mining techniques. These studies can help to speed up and computerize the process of crime analysis processes. However the pattern of crime is not static, it always change and growth [7].

With social media, users post and discuss event publicly. These textual data of every user's post has contextual information of user's daily activities. These posts generate unstructured data that can be used for crime prediction. Previous researches had shown that twitter sentiment enable to predict crime in Chicago, United States. However, existed models on crime prediction present only sentiment analysis on twitter content with Kernel Density Estimation of historical crime. The models are lack of applying socio factors. In contrast, crime prediction model will produce more significant if socio-factor is added to sentiment analysis and KDEs.

Therefore, the study aims to fulfill the gap mention above by considering socio-factor especially gender, age and education level to be significantly influent factor that could lead a person commit crime. The paper is structured as follows: Section 2 discusses related work. Selection 3 discuses the development of prediction model. Section 4 presents model evaluation, and section 5 is the conclusion.

2. Related study

2.1. Crime Prediction

Hot-spot maps are a traditional method of analyzing and visualizing the distribution of crimes across space and time [8]. Relevant techniques include Kernel Density Estimation (KDE), which fits a two-dimensional spatial probability density function to a historical crime record. This approach allows the analyst to rapidly visualize areas with historically high crime concentrations. Future crimes often occur in the vicinity of past crimes; therefore making hot-spot maps is a valuable crime prediction tool. KDEs are a model that has been applied for crime detection base on history of crime data. It displays higher risk in area for higher density of crime. KDEs consist of ArcGIS, MapInfo, R, and CrimeStat III that is applicable for crime hotspot detection. To improve the performance of crime detection and prediction, KDEs recently use spatial, temporal, and social media data [9][1][10].

More advanced techniques like self-exciting point process models also capture the spatiotemporal clustering of criminal events [11]. These techniques are useful but carry specific limitations. First, they are locally descriptive, meaning that a hot-spot model for one geographic area cannot be used to characterize a different geographic area. Second, they require historical crime data for the area of interest, meaning they cannot be constructed for areas that lack such data. Third, they do not consider the rich social media landscape of an area when analyzing crime patterns.

Researchers have addressed the first two limitations of hot-spot maps by projecting the criminal point process into a feature space that describes each point in terms of its proximity to, for example, local roadways and police headquarters [12]. This space is then modeled using simple techniques such as generalized additive models or logistic regression. The benefits of this approach are clear: it can simultaneously consider a wide variety of historical and spatial variables when making predictions; furthermore, predictions can be made for geographic areas that lack historical crime records, so long as the areas are associated with the requisite spatial information (e.g., locations of roadways and police headquarters). The third limitation of traditional hot-spot maps; the lack of consideration for social media has been our objective in our research.

2.2. Prediction via social media using sentiment analysis

In a forthcoming survey of social-media-based predictive modeling, Kalampokis et al. identify seven application areas represented by 52 published articles [13]. As shown, researchers have attempted to use social media to predict or detect disease outbreaks [14], election results [15], macroeconomic processes (including crime) [16], box office performance of movies [17], natural phenomena such as earthquakes [18], product sales [19], and financial markets [20]. These researches primarily use the technique of sentiment analysis. Researchers employ semantic analysis on the contextual contents of each tweet and draw the predictive response of the selected group of people.

A primary difference between nearly all of these studies and the present research concerns spatial resolution. Whereas processes like disease outbreaks and election results can be addressed at a spatial resolution that covers an entire city with a single prediction, criminal processes can vary dramatically between individual city blocks. The work by Wang et al. comes closest to the present research by using tweets drawn from local news agencies [16]. The authors found preliminary evidence that such tweets can be used to predict hit-and-run vehicular accidents and breaking-and entering crimes; however, their study did not address several key aspects of social-media-based crime prediction. First, they used tweets solely from hand-selected news agencies. These tweets, being written by professional journalists, were relatively easy to process using current text analysis techniques; however, this was done at the expense of ignoring hundreds of thousands of potentially important messages. Second, the tweets used by Wang et al. were not associated with GPS location information, which is often attached to Twitter messages and indicates the user s location when posting the message. Thus, the authors were unable to explore deeper issues concerning the geographic origin of Twitter messages and the correlation between message origin and criminal processes. Third, the authors only investigated two of the many crime types tracked by police organizations, and they did not compare their models with traditional hot-spot maps.

In our study, we addressed these limitations. We applied sentiment analysis to evaluate the polarity of tweets. We also integrated socio-economic factors into the model with sentiment polarity and historical crime record as explanatory variables. Taking full advantage of all these features, we are able to develop more accurate prediction on future crime incidents.

3. Prediction model

To construct crime model, Frist, we define training set of crime density, data from twitter and data of socio-factors. These data contain location where crime is occurred (latitude and longitude) within a specific training window (for example: 1January 2018 – 31 January 2018). The location of spatial points are designed whether they have crime or not within 200qm. Therefore, a city of training set is divided into multitude of smaller region with length of 200qm. All crime points are then assigned to small sectors (neighborhoods). At this step we have a binary classifiers to determine crime and non-crime point. Second, we collect data from twitter with a specific latitude/longitude and training window as mention above. The data contain two parts; first tweet post and second socio factor-that we can derive from user profile such as gender, age and employment status. Tweet will be computed to find polarity score of sentiment analysis. Last, we combine socio-factor, tweet polarity score with crime density. Let us have variable as following:

Response Variable
$X_t(p)$ = Crime or non-crime point (0 is non-crime and 1 is crime point)

Explanatory variable
Explanatory variable
$f_1(p)$ = Density of past crime
$f_2(p)$ = Tweet polarity score (-1 to 1)

$f_3(p)$ = Trend of polarity score
$f_4(p)$ = Gender
$f_5(p)$ = Age
$f_6(p)$ = Employment status

3.1. Historical crime density $f_1(p)$

To calculate historical density of a particular type of crime (for example theft crime) at p point, let take $f_1(p)$ be Kernel Density Estimation (KDE) at point p:

$$f_1(p) = k(p,h) = \frac{1}{Ph}\sum_{j=1}^{k} K\left(\frac{\|p-p_j\|}{h}\right) \tag{1}$$

From Eq.(1), we have p is the point that we need to calculate the crime density, set h to be parameter (or bandwidth) to control the smoothness of density, P is total number of a crime (theft crime from the example) that occur in the city, set j to index a single point of crime, K is the function of density (we can use standard normal density function), $||.||$ is the Euclidean norm, p_j is the actual point of crime (theft) in the city. To help calculation of $k(p,h)$, we can use ks packaged in R software, and we can also use Hpi function to get values of h.

3.2. Information messages from Twitter $f_2(p)$

Messages from Twitter will be collected within a specific latitude/longitude and training window of time. At this point, the spatial sectors (neighborhood) lay down to 1000 x 1000 meter. Within defined spatial sectors (neighborhood) above, we are able to find polarity score of sentiment base on given tweet message from users in each sector. Polarity function and Sentiment Lexicon Dictionary will be used to perform for this purpose.

Once we find sentiment polarity, we then find sentiment trend in each neighborhood, because it intuitively cause higher risk of crime. To measure sentiment trend, let take $f_3(p)$ as trend of polarity score, X_i is the percentage of change between previews k of period's polarity and today's polarity is:

$$V_i = \sum_{j=1}^{k} \left(\frac{p_{i-j}-p_j}{p_j}\right) \tag{2}$$

If the period is changed over 10%, we get sum of the change for $f_3(p)$ as follows:

$$=T_i = \sum_v \{v \in V_i : v > 10\% \cup v < 10\%\} \tag{3}$$

If the value of T is positive, the polarity of preview period is greater than polarity of current period. And if T is negative, the polarity of current period is greater than preview period.

3.3. Logistic Regression

In order to predict future crime that may occur, we define $X_{t+1}(p)$ to determine whether crime will occur in p neighborhood on the next day. Full form of logistic regression is shown in Eq.(4).

$$log\left\{\frac{Pr[x_{t+1}(p)=1]}{1-Pr[x_{t+1}(p)=1]}\right\} = \beta_0 + \beta_1 f_{t,1}(p) + \cdots + \beta_6 f_{t,6}(p) \tag{4}$$

$(\beta_0 \dots \beta_6)$ can be calculated by using maximum likelihood function of historical crime (for example theft crime).

Our objective is to develop a model to predict crime incident using Twitter sentiment polarity, socio-factor on KDE model. We first estimate historical crime density on each neighborhood p at time t using KDE as mention in Eq.(1). We then calculate polarity of tweets and its trend at each neighborhood p as mention in Eq.(2) and Eq.(3). Logistic regression model is then performing density estimation, feature from Twitter and socio-factor to forecast the probability of crime incident on next day t+1 in each point.

4. MODEL EVALUATION

To measure the performance of logistic regression, we use surveillance plots. Surveillance plots measures a crime as percentage of capture on y-axis of prediction window per percentage captured area for a particular crime prediction. If the value of sentiment polarity is increasing, the higher rate a crime could be occurred. The function of capture crime and captured area is written as:

$$\%\ \text{Area Surveilled} = x\% = \frac{\sum_{i=1}^{s} A_i}{\sum_{i=1}^{n} A_i} \tag{5}$$

$$\%\ \text{Crime Captured} = y\% = \frac{\sum_{i=1}^{s} C_i}{\sum_{i=1}^{n} C_i} \tag{6}$$

where $\{A_n\}$ is the capture area sorted by point p, $\{c_i\}$ is the capture crime with captured area, and s is the number of capture area. From this equation, we derive function of surveillance curve (AUC) as:

$$\mathrm{AUC} = \int_{-\infty}^{\infty} y(A) * x'(A) dA \tag{7}$$

Meaning that, in order to evaluate prediction model we use AUC of prediction performance then compare with benchmarked logistic regression model.

5. Conclusion

In this paper we have presented the model development of crime prediction using sentimental contents, socio-factor with crime density estimation. Few researches have explained the correlation between crime and sentiment and none has taken into account these together in model construction. Therefore, this research fulfills this gab. However, this research present only initial model development, we are planning to further improve it with real training data set.

References

[1] Matthew, S. G., Predicting crime using twitter and kernel density estimation, *Decision Support Systems,* 61 (2014), 115–125.

[2] Twitter, TWITTER USAGE / COMPANY FACTS, Retrieved from http://www.twitter.com Retried on November 1, 2017

[3] Salim A. and Omer, E., Cybercrime Profiling: Text mining techniques to detect and predict criminal activities in microblog posts, *International Conference on Intelligent Systems: Theories and Applications* (SITA), (2015) 1-5.

[4] Vieweg, S., Hughes, A. L., Starbird K. and Palen, L., Microblogging during two natural hazards events: what twitter may contribute to situational awareness, *SIGCHI Conference on Human Factors in Computing Systems*, (2010) 1079–1088.

[5] Tumasjan, A., Sprenger, T. O., Sandner, P. Q. and Welpe, I. M., Predicting elections with twitter: What 140 characters reveal about political sentiment. *ICWSM,* 10 (2010),178–185.

[6] Xiaofeng, W., Matthew S. G. and Donald, E. B., Automatic crime prediction using events extracted from twitter posts. Social Computing, *Behavioral-Cultural Modeling and Prediction*, (2015) 231–238.

[7] Sathyadevan, S., Devan M. and Surya, S., Gangadharan, Crime analysis and prediction using data mining, *Networks Soft Computing (ICNSC),* (2014) 406–412.

[8] Chainey, S., Tompson, L. and Uhlig, S., The utility of hotspot mapping for predicting spatial patterns of crime, *Security Journal*, 21(2008), 4–28.

[9] Caplan, J.M. and Kennedy, L.W., Risk terrain modeling compendium. *Rutgers Center on Public Security*, Newark, (2011).

[10] Mohammad A.B. and Matthew, S.G., Predicting Crime with Routine Activity Patterns Inferred from Social Media. *International Conference on Systems, Man, and Cybernetics – SMC*, (2016), 1233-1238.

[11] Mohler, G.O., Short, M.B., Brantingham, P.J., Schoenberg F.P. and Tita, G.E., Self-Exciting Point Process Modeling of Crime. *Journal of the American Statistical Association,* 106 (2011), 100-108.

[12] Xue, Y. and Brown, D.E., Spatial analysis with preference specification of latent decision makers for criminal event prediction, *Decision Support Systems*, 41 (2006), 560–573.

[13] Kalampokis, E., Tambouris, E., and Tarabanis, K., Understanding the predictive power of social media, *Internet Research*, 23 (2013).

[14] Culotta, A. and Huberman. B., Towards detecting influenza epidemics by analyzing Twitter messages, *Proceedings of the First Workshop on Social Media Analytics, ACM*, (2010) 115–122.

[15] Franch, F., Wisdom of the crowds 2: 2010 UK election prediction with social media, *Journal of Information Technology & Politics,* 10 (2013), 57–71.

[16] Wang, X., Brown, D. and Gerber, M., Spatio-temporalmodeling of criminal incidents using geographic, demographic, and Twitter-derived information, *Intelligence and Security Informatics.* Lecture Notes in Computer Science, IEEE Press, (2012).

[17] Asur, S. and Huberman, B., Predicting the future with social media, *IEEE/WIC/ACM International Conference on Web Intelligence and Intelligent Agent Technology, IEEE*, (2010) 492–499.

[18] Earle, P.S., Bowden, D.C. and Guy, M, Twitter earthquake detection: earthquake monitoring in a social world, *Annals of Geophysics*, 54 (2012).

[19] Choi, H,. and Varian, H., Predicting the present with Google Trends, *The Economic Record*, 88 (2012), 2–9.

[20] Bollen, J., Mao H., Zeng, X., Twitter mood predicts the stock market, *Journal of Computational Science,* 2(2011), 1–8.

Current Address: Sakirin TAM: Department of Computer Engineering, Ankara University, Ankara 06830, TURKEY
E-mail Address: *kirin.it@gmail.com*
ORCID: https://orcid.org/0000-0003-4103-1797

Current Address: Ö. Özgür TANRIÖVER: Department of Computer Engineering, Ankara University, Ankara 06830, TURKEY
E-mail Address: *tanriover@ankara.edu.tr, tanriove*r@yahoo.com
ORCID: https://orcid.org/0000-0003-0833-3494

Commun.Fac.Sci.Univ.Ank.Series A2-A3
Volume 60, Number 1, Pages 21-30(2018)
DOI: 10.1501/commua1-2_0000000108
ISSN 1303-6009 E-ISSN 2618-6462
http://communications.science.ankara.edu.tr/index.php?series=A2A3

CONTROL OF COLLECTIVE BURSTING IN SMALL HODGKIN-HUXLEY NEURON CLUSTERS

SERGEY BORISENOK, ÖNDER ÇATMABACAK, AND ZEYNEP ÜNAL

Abstract. The speed gradient-based control algorithm for tracking the membrane potential of Hodgkin-Huxley neurons is applied to their small clusters modeling the basic features of an epileptiform dynamics. One of the neurons plays a role of control element detecting the temporal hyper-synchronization among its network companions and switching their bursting behavior to resting. The 'toy' model proposed in the paper can serve as an algorithmic basement for developing special control elements at the scale of one or few cells that may work autonomously and are able to detect and suppress epileptic behavior in the networks of real biological neurons.

1. Introduction

Epilepsy is a disease involving changes at multiple different spatial and temporal scales and, therefore, demands for its modeling such a basic neuron mathematical element that possesses many degrees of freedom, like Hodgkin-Huxley (HH) neurons [1]. The chains of many HH neurons in the epileptiform regime demonstrate good agreement with animal in vivo recordings [2,3]. The synchronization/desynchronization of the cell behavior in the neural networks is the sufficient phenomenon for the understanding the mechanism of epilepsy [4,5]. Modern neuroscience demonstrates a great progress in study of the collective chaotic regimes of biological neurons, but its mathematical modeling still needs a sufficient improvement [6]. The Hodgkin-Huxley's system covers some possible scenarios of the appearance of the collective bursting: ion channel mutations and fluctuations in concentration gradient of ions from inside to outside the axon [7].

Recently we've developed the efficient algorithm to track an arbitrary dynamical regime in a single HH neuron controlled by an external electrical signal [8]. Here Fradkov's speed gradient feedback [9] is applied to suppress the collective bursting

---

Received by the editors: November 10, 2017; Accepted: January 27, 2018.
Key word and phrases: Neuroinformatics, Hodgkin-Huxley neuron, speed gradient feedback, collective bursting control, epileptiform dynamics.
This work has been supported by the TÜBİTAK project 116F049 "Controlling Spiking and Bursting Dynamics in Hodgkin-Huxley Neurons".

in the small clusters of Hodgkin-Huxley neurons via the driving action potentials in the neural axons. Our tracking algorithm allows to detect the hyper-synchronized dynamics in the cluster and to transfer the behavior of some selected neurons from the collective bursting to the resting.

The control is performed with the single element of the cluster via the feedback to its bursting companions. The proposed algorithm can be used efficiently for studying, detecting and suppressing the epileptiform behavior [7] of spiking and bursting in the models for biological neuronal networks.

2. SPEED GRADIENT FEEDBACK CONTROL FOR HODGKIN-HUXLEY NEURONS

To model the basic element of the neural cluster we use here the Hodkin-Huxley (HH) model proposed in [1]. The k-th neuron in the population is described by the dynamical set of ordinary differential equations:

$$\begin{aligned}
&C_M \cdot \frac{dv_k}{dt} = -g_{Na} m_k^3 h_k \cdot (v_k - E_{Na}) - g_K n_k^4 \cdot (v_k - E_K) - g_{Cl} \cdot (v_k - E_{Cl}) + I_k(t)\ ;\\
&\frac{dm_k}{dt} = \alpha_m(v_k) \cdot (1 - m_k) - \beta_m(v_k) \cdot m_k\ ;\\
&\frac{dn_k}{dt} = \alpha_n(v_k) \cdot (1 - n_k) - \beta_n(v_k) \cdot n_k\ ;\\
&\frac{dh_k}{dt} = \alpha_h(v_k) \cdot (1 - h_k) - \beta_h(v_k) \cdot h_k\ .
\end{aligned} \qquad (2.1)$$

Here *vk(t)* stands for the action potential of the axon, *mk(t), nk(t), hk(t)* are its membrane gate variables. The summary current Ik(t) entering the k-th cell plays a role of an external signal stimulating spiking or bursting dynamics of the neuron. αm,n,h, βm,n,h are fenomenologically found functions related to the membrane gate probabilities and given by [1]:

$$
\begin{aligned}
&\alpha_m(v)=\frac{0.1\cdot(25-v)}{\exp\left\{\dfrac{25-v}{10}\right\}-1}\,;\ \beta_m(v)=4\cdot\exp\left\{-\frac{v}{18}\right\};\\
&\alpha_n(v)=\frac{0.01\cdot(10-v)}{\exp\left\{\dfrac{10-v}{10}\right\}-1}\,;\ \beta_n(v)=0.125\cdot\exp\left\{-\frac{v}{80}\right\};\\
&\alpha_h(v)=0.07\cdot\exp\left\{-\frac{v}{20}\right\};\ \beta_h(v)=\frac{1}{\exp\left\{\dfrac{30-v}{10}\right\}+1}\,.
\end{aligned}
\tag{2.2}
$$

The set of constants in (2.1) includes the potentials ENa (equilibrium potential at which the net flow of Na ions is zero), EK (equilibrium potential at which the net flow of K ions is zero), ECl (equilibrium potential at which leakage is zero) in mV, the membrane capacitance CM and the conductivities gNa (sodium channel conductivity), gK (potassium channel conductivity), gCl (leakage channel conductivity) in mS/cm2:

$$
\begin{aligned}
&g_{Na}=120;\ E_{Na}=115\,;\\
&g_K=36;\ \ E_K=-12\,;\\
&g_{Cl}=0.3;\ E_{Cl}=10.36\,.
\end{aligned}
\tag{2.3}
$$

The link element transfers the electrical stimulation from the axon of (k −1)-th neuron to the input of k-th neuron via synapses, dendrites and soma of the k-th cell. We use the gain model:

$$
I_k(t)=\alpha\cdot[v_{k-1}(t)-v_{\mathrm{rest}}]\,;\ \alpha=\mathrm{const}>0,
\tag{2.4}
$$

where the reference rest potential of an HH neuron is given by [1]:

$$
\begin{aligned}
&v_{\mathrm{rest}}=58\log\left(\frac{P_K\cdot K_{\mathrm{ext}}+P_{Na}\cdot Na_{\mathrm{ext}}+P_{Cl}\cdot Cl_{ext}}{P_K\cdot K_{\mathrm{int}}+P_{Na}\cdot Na_{\mathrm{int}}+P_{Cl}\cdot Cl_{\mathrm{int}}}\right);\\
&K_{\mathrm{ext}}=20;\ K_{\mathrm{int}}=400;\\
&Na_{\mathrm{ext}}=440;\ Na_{\mathrm{int}}=50;\\
&Cl_{\mathrm{ext}}=560;\ Cl_{\mathrm{int}}=150;\\
&P_K=1;\ P_{Na}=3;\ P_{Cl}=0.45\,.
\end{aligned}
\tag{2.5}
$$

The algorithm for tracking the membrane potential v(t) in a single neuron have been developed in [8]. For a single element tracking provides the reproduction of an arbitrary target function v*(t) by the potential v(t) via the designing the control current ISG(t). To do it, let's define the scalar target (goal) function of the HH neuron as:

$$G = \frac{1}{2}\left[v(t) - v_*(t)\right]^2 . \tag{2.6}$$

The speed gradient algorithm [9] defines the gradient control in the space of the control signal. In the case of single neuron it is reduced to the partial derivative:

$$I_{\mathrm{SG}}(t) = -\gamma \frac{\partial}{\partial I}\left(\frac{dG}{dt}\right). \tag{2.7}$$

Here is a positive constant. For the HH model (2.1) the algorithm (2.7) implies [8]:

$$I_{\mathrm{SG}}(t) = -\frac{\gamma}{C_M}[v(t) - v_*(t)] \, . \tag{2.8}$$

Together with the dynamical set (2.1)-(2.4) Eq.(2.8) forms the control model for the HH cluster.

3. Control model of the epileptiform suppression

In this paper we introduce a basic 'toy' model for the epileptiform suppression. Let's consider the sub-cluster of three HH neurons, see the configuration on Figure 1.

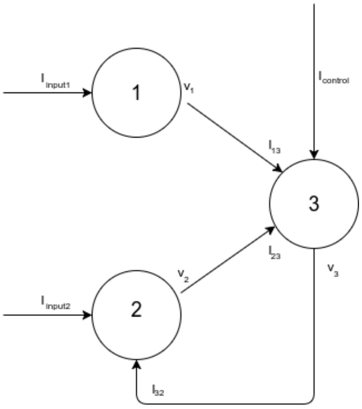

FIGURE 1. Basic model for an epileptiform suppression in the cluster of three Hodgkin-Huxley neurons.

Here the neurons 1 and 2 are involved into the collective bursting stimulated by the currents Iinput1 and Iinput 2 coming from other companion cells in the neural population. The neuron 3 is a monitoring element providing the switch on and off for the algorithm of suppression. It plays two roles. First, it detects the over-synchronization of the signals coming from the neurons 1 and 2 through the input currents I13 and I23 (sure, the neurons 1 and 2 may also stimulate other neurons in the bigger cluster, they are not shown on Figure 1). Second, if the neuron 3 observes the over-synchronization in a certain interval of time, it triggers the control algorithm of the suppression through the feedback loop to the neuron 2 by the current I32. The control current Icontrol reflects the inner degree of freedom for the neuron 3. Thus, this element works as an automat driving the neuron 2 from the bursting regime to the resting if and only if it detects its over-synchronization with the neuron 1.

The basic cluster configuration on Figure 1 can be written in the form of coupled differential equations of (2.1)-type:

$$
\begin{aligned}
&C_M \cdot \frac{dv_1}{dt} = -g_{Na} m_1^3 h_1 \cdot (v_1 - E_{Na}) - g_K n_1^4 \cdot (v_1 - E_K) - g_{Cl} \cdot (v_1 - E_{Cl}) + \\
&\qquad + I_{\text{input1}} \; ; \\
&C_M \cdot \frac{dv_2}{dt} = -g_{Na} m_2^3 h_2 \cdot (v_2 - E_{Na}) - g_K n_2^4 \cdot (v_2 - E_K) - g_{Cl} \cdot (v_2 - E_{Cl}) + \\
&\qquad + I_{\text{input2}} + I_{31} \; ; \\
&C_M \cdot \frac{dv_3}{dt} = -g_{Na} m_3^3 h_3 \cdot (v_3 - E_{Na}) - g_K n_3^4 \cdot (v_3 - E_K) - g_{Cl} \cdot (v_3 - E_{Cl}) + \\
&\qquad + I_{13} + I_{23} + I_{\text{control}} \; ; \\
&\frac{dm_k}{dt} = \alpha_m(v_i) \cdot (1 - m_k) - \beta_m(v_k) \cdot m_k \; ; \\
&\frac{dn_k}{dt} = \alpha_n(v_k) \cdot (1 - n_k) - \beta_n(v_k) \cdot n_k \; ; \\
&\frac{dh_k}{dt} = \alpha_h(v_k) \cdot (1 - h_k) - \beta_h(v_k) \cdot h_3 \; ; \; k = 1,2,3,
\end{aligned}
\tag{3.1}
$$

with the synaptic links:

$$
\begin{aligned}
I_{13}(t) &= \alpha \cdot [v_1(t) - v_{\text{rest}}] \; ; \\
I_{23}(t) &= \alpha \cdot [v_2(t) - v_{\text{rest}}] \; ; \\
I_{31}(t) &= \alpha \cdot [v_3(t) - v_{\text{rest}}] \; .
\end{aligned}
\tag{3.2}
$$

Here we use our method of 'back spread' algorithmic goal: the real control signal is passing from the neuron 3 to the neuron 2, while the algorithmic definition of the goal follows the opposite direction, from 2 to 3, see Eqs.(3.5)-(3.7) below.

First, we apply SG algorithm (2.8) to the neuron 3:

$$
I_{\text{control}}(t) = -\gamma \cdot [v_3(t) - v_{3*}(t)] \; . \tag{3.3}
$$

The goal v3* of the tracking potential in the neuron 3 is defined as the inverse function to (2.4):

$$
v_{3*}(t) = \frac{I_{31*}(t)}{\alpha} + v_{\text{rest}} \; . \tag{3.4}
$$

The control current Icontrol entering the neuron 3 is given also in the SG form (2.8):

$$I_{31*}(t) = -\gamma \cdot \Delta\big(I_{13}(t) - I_{23}(t)\big) \cdot [v_2(t) - v_{rest}] \ , \tag{3.5}$$

where Δ stands for the smooth model of delta-function:

$$\Delta(x) = \frac{1}{\sqrt{\pi}d} \exp\left\{-\frac{x^2}{d^2}\right\} \ ; \ d = \text{const} > 0 \ . \tag{3.6}$$

The factor Δ in (3.5) switches on the control algorithm only for the synchronized currents I13 and I23, and in the case of their time over-synchronization, i.e. only in the period of their epileptiform dynamics, leads the neuron 2 to the stabilization at the rest membrane potential.

This algorithm can be easily extended for a larger number of collective bursting neurons and their feedback links in the population.

4. Numerical simulations

For the purpose of numerical simulations the following set of parameters has been chosen:

$$I_{\text{input1}} = 50 \ ; I_{\text{input2}} = 50 \ ; \ \alpha = 10 \ ; \ \gamma = 50 \ ; \ C_M = 1 \ ; \ d = 0.1 \ . \tag{4.1}$$

The results of the simulation are presented on Figure 2.

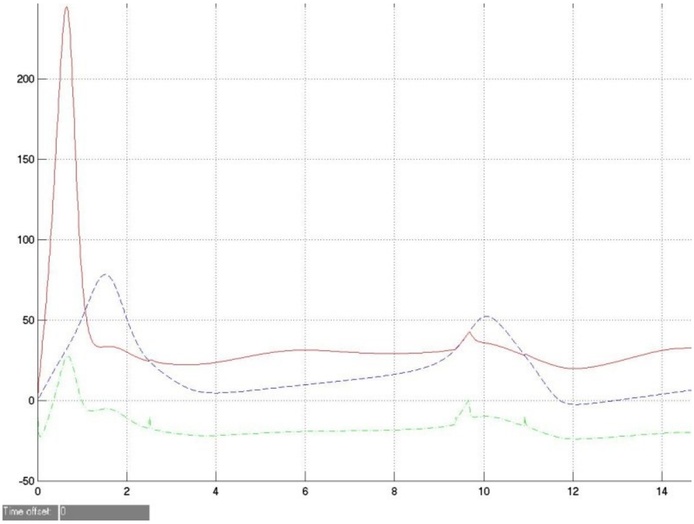

FIGURE 2. The neuron membrane potentials v1 (blue dashed line), v2 (red solid line) and v3 (green dash-dotted line) vs time.

On the Figure 2 one can see that after the beginning instability at the scale t = 2 the potential v2 is suppressed approximately in two times to compare with the bursting potential v1. This result seems to be very good for such a simple control model. When the collectively synchronized bursting is starting to growth (closed to t = 10), the control mechanism is switching on to drive the potential of the neuron 2 far away from the synchronization. The same is happen when t = 12.

Sure, the presented algorithm reflects only the basic features of the bursting suppression. The 'toy' control (3.5)-(3.6) needs to be sufficiently improved for the better detecting the chaotic hyper-synchronization in the clusters and feating more flexible details of the neuron dynamics.

5. CONCLUSIONS

The control algorithm developed in [8] for tracking the membrane potential of a single Hodgkin-Huxley neuron can be applied to a small configuration of HH elements modeling the basic features of an epileptiform dynamics. In this population one of the neurons plays a role of control element detecting the temporal hyper-synchronization among its network companions and switching on the feedback signal that it sends to some selected neurons in the population to drive them off the epileptiform regime.

The ‘toy’ model proposed in the paper can serve as an algorithmic basement for developing special control elements at the scale of one or few cells that may work autonomously and are able to detect and suppress epileptic behavior in the networks of real biological neurons.

Acknowledgments

This work has been supported by the TÜBİTAK project 116F049 “Controlling Spiking and Bursting Dynamics in Hodgkin-Huxley Neurons”.

References

[1] Hodgkin and A.L. Huxley, A.A., Journal of Physiology, 117 (1952), 500-544.

[2] Rubio, C, Rubio-Osornio, M., Retana-Márquez, S., López, M., Custodio, V. and Paz, C., *Central Nervous System Agents in Medicinal Chemistry*, 10/4 (2010) 298-309.

[3] Naze, S. Bernard and Ch. Jirsa, V., PLOS *Computational Biology*, 1 (2015) 1-21.

[4] Reynolds, E.H., Epilepsy: The disorder, (Epilepst Atlas, WHO, 2005, 16-27).

[5] Eftaxias, K. Minadakis, G. Athanasopoulou, L. Kalimeri, M. Potirakis, S.M. and Balasis, G., Are epileptic seizures quakes of the brain? An approach by means of nonextensive Tsallis statistics, 2011, *arXiv preprint* arXiv:1110.2169.

[6] Petkov, G., Goodfellow, M., Richardson, M. P. and Terry, J., *Frontiers in Neurology*, 5 (2014) 261.

[7] Wendling, F., Benquet, P., Bartolomei and F. Jirsa, V., *Journal of Neuroscience Methods*, 260 (2016) 233-251.

[8] Borisenok, S. and Ünal, Z., MATTER: *International Journal of Science and Technology*, 3/2 (2017) 560-576.

[9] Fradkov, A.L., Cybernetical physics: From control of chaos to quantum control, Springer, Berlin, 2007.

Current Address: Sergey BORISENOK: Department of Electrical and Electronics Engineering, Faculty of Engineering, Abdullah Gül University, Kayseri, Turkey
Sergey BORISENOK: Feza Gürsey Center for Physics and Mathematics, Boğaziçi University, Istanbul, Turkey
E-mail: sergey.borisenok@agu.edu.tr, borisenok@gmail.com
ORCID: https://orcid.org/0000-0002-1992-628X

Current Address: Önder ÇATMABACAK: Faculty of Engineering and Natural Sciences, Sabancı University, Istanbul, Turkey
E-mail Address: ondercatmabacak@gmail.com
ORCID: https://orcid.org/0000-0002-6419-0363

Current Address: Zeynep ÜNAL: Department of Electrical and Electronics Engineering, School of Engineering, Abdullah Gül University, Kayseri, Turkey
E-mail Address: zeynepsenel51@gmail.com
ORCID: https://orcid.org/0000-0002-4640-4049

Commun.Fac.Sci.Univ.Ank.Series A2-A3
Volume 60, Number 1, Pages 31-40 (2018)
DOI: 10.1501/commua1-2_0000000109
ISSN 1303-6009 E-ISSN 2618-6462
http://communications.science.ankara.edu.tr/index.php?series=A2A3

CELL OUTAGE DETECTION IN LTE-A CELLULAR SYSTEMS USING NEURAL NETWORKS

HASAN TAHSİN OĞUZ AND AYKUT KALAYCIOĞLU

Abstract. Self-organizing networks (SONs) are considered as one of the key features for automation of network management in new generation of mobile communications. The upcoming fifth generation (5G) mobile networks are likely to offer new challenges for SON solutions. In SON structure, self-healing is an outstanding task which comes along with Cell Outage Detection (COD) and Cell Outage Compensation (COC). This study investigates the detection of cell outages by means of the metrics generated in the User Equipment (UE) with the help of pattern recognition methods such as Neural Networks, Logistic Regression and k-Means algorithms. Based on the metrics like Signal to Interference Noise Ratio (SINR), Reference Signal Received Quality (RSRQ), and Channel Quality Indicator (CQI), large amount of data is processed with supervised and unsupervised algorithms for the purpose of classifying outages and possible degradations. Our results suggest that in 79.74% of the simulation cases, Neural Network structure was able to identify the correct state of the cells whether it is outage or not with a true positive rate of 87.61% and a true negative rate of 71.87% whereas Logistic Regression gave a success rate of 78.73%, true positive rate of 88.15%, and true negative rate of 69.3%. As a future work, more sophisticated state-of-the-art deep learning mechanisms can lead us to much more successful results in cell outage detection.

1. Introduction

Next generation 5G systems is supposed to bring in ultra-dense deployments for the purpose of attaining more capacity, higher rates, ultra-low latency, massive connectivity and lower energy consumption. For better network maintenance, Third-Generation Partnership Project (3GPP) has already set forth the concept of Self Organizing Networks (SON) which involves Self-Configuration, Self-Optimization and Self-Healing. Cell Outage Detection is the first primary step for Self-Healing feature of the future 5G Self Organizing Networks. Hardware or software failures or external failures such as power supply or network connectivity are the main causes for outages. Cell outage is defined as a state of the eNodeB where all or most of the User Equipment (UEs) in the cell are unable to establish or keep its radio

---

Received by the editors: April 06, 2018; Accepted: May 21, 2018.
Key word and phrases: Cell outage detection, neural networks, 5G, self-organizing networks.

connectivity with the result of reduction in capacity and coverage gaps. Especially in the existence of dense deployments, outages may not be detected for hours or even days. Traditionally, detection outages may require site visits, drive tests and manual analysis of the alarms generated on the Operations and Support Systems (OSS) which makes outage detection costly [1].

Cell Outage Detection (COD) is basically a binary classification problem to detect the degraded cell among healthy ones by making use of some UE statistics reported to the eNodeB. Future 5G mobile networks are supposed to handle COD autonomously. Therefore, detection algorithms employed on the Operations and Support System (OSS) should online monitor the UE statistics continuously and process the data measured on the UEs as suggested by 3GPP releases [2].

In previous studies, algorithms based on the spatial correlations among users have been used in cell outage detection [3]. Handover statistics were also employed on COD analysis [4]. In [5] COD has been handled via employing neighbor cell list reports and detecting outage cells by looking at the changes in the topology generated by visibility graphs. In [6], Channel Quality Indicator (CQI) based composite hypothesis has been utilized for outage detection. Machine learning has also been popular in outage detection. In [7] and [8], clustering algorithms and Bayesian Networks have been conducted for COD respectively. Hidden Markov Models (HMM), as another well-known classifier, was also studied in COD by training the data regarding healthy cells and outage cells for predicting the outage status of the eNodeBs [9]. K-Nearest Neighbors method has been conducted in [10] for COD in multi-tier networks. In [11], alternative to machine learning procedures, an anomaly detection method based on processing of big data emerged from Key Performance Indicators (KPI) has been introduced.

In this study, feed forward Multilayer Perceptron (MLP) type artificial Neural Networks are used for detection of cell outages in a network of eNodeBs. Neural Networks (NN) is one of the novel pattern recognition tools that have been used on many areas so far. Thereby, we employed supervised NN for the investigation of outage patterns based on the metrics measured on UEs placed in the cell. In this study we have used the metrics SINR, CQI and RSRQ as the input for the NN structure by training the system at the beginning and then applying the test data.

The rest of the paper is organized as follows. In Section 2 the metrics and parameters for outage detection are briefly discussed. In Section 3, the details of the artificial Neural Network application and training scheme are introduced. Section 4 presents the results in a comparative manner along with other classification methods like

Logistic Regression and k-Means algorithms. Finally, we conclude the paper in Section 5.

2. Algorithm Description

The eNodeBs in the cellular wireless systems in this study are considered to be in two states as healthy and outage. Outage cells and healthy cells are assumed to radiate with a power of 0 dBm and 46 dBm respectively. Due to some reasons such as hardware or software failures, external power supply problems or even misconfiguration, and etc., when the output power of the eNodeB degrades, the cell goes into outage state. However service providers generally cannot realize these types of state changes very quickly and efficiently. Making use of the measured UE data related to received signal strength, which are also reported to eNodeBs, the outage state might be detected by use of artificial neural networks which have been employed in many fields so far. Therefore, feed forward artificial neural networks are preferred in this study for COD.

Feed forward neural networks are used in this study. Feed forward networks consist of series of neuron layers. The first layer has a connection from the network input. Each subsequent layer of neurons has a connection from the previous layer. The output layer is the last layer of the structure and the layers other than the output layer are hidden layers. Feed forward networks are suitable for mapping any finite-input finite-output problems. In our case some KPIs (Key Performance Indicator) are chosen as the input to the network and the output is the Boolean data regarding the outage.

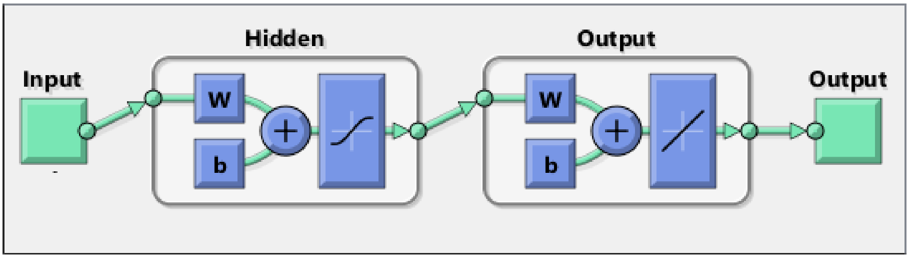

Figure 1. Structure of a feed-forward network

In feed forward neural networks data is fed into the network from input layer. The output is computed according to the equation (1). In equation (1), X, W, Y, and T are the input, weight, output and threshold matrices, respectively. Besides, denoted both in equation (1) and (2), f is the activation function.

$$Y = f(W \times X - T) \tag{1}$$

$$f(X) = \frac{1}{1+e^X} \tag{2}$$

In this scheme, a weight adjustment process takes place in such a way that the weights are updated in every iteration until the desired output is achieved with an error of less than a threshold with the error fed back layer by layer. The adjustment of the weights is the training process for the neural network to accomplish the learning goal.

2.1. Detection Parameters

For the purpose of Cell Outage Detection we made use of some KPIs within Artificial Neural Networks (ANNs). The KPIs are collected from several sources like User Equipment, eNodeBs and Operation Support Systems. The combination of KPIs may provide critical information for accurate detection of a possible degradation on the cellular system. We have selected SINR, CQI and RSRQ as the parameters to work on. SINR is basically the signal to interference plus noise ratio of a UE. CQI is the channel quality indicator carrying information about the channel quality of the communication link. Third metric reference signal received quality (RSRQ), as the name implies, indicates the received quality of the reference signal. RSRQ is used for handover decisions and cell re-selection. In this study we made use of these three metrics measured on the UEs. With these parameters from the UEs being the inputs for the Neural Network, we trained the network and then tested the network for healthy and outage cases.

2.2. Training and Detection Procedure

Prior to detecting the outages, Neural Network structure should be trained so as to learn the patterns on healthy and outage states. For every UE on the site, the three parameters (SINR, CQI, and RSRQ) are collected for healthy and outage cases so that an input data of three features are provided. The input data matrix is fed into a feed-forward back propagation Neural Network. After training the net, test data regarding the outage and healthy cases are fed into the Neural Network structure as inputs and the resulting success is measured accordingly. The data structure input to the Neural Network is shown in Figure 2. Assuming M number of UEs on the site there is an input data matrix of dimension $Mx3$ and there is also a state matrix which have binary values either 1 or 0 indicating an outage or not, respectively.

$$\begin{array}{ccc}
\textbf{User} & \textbf{Data} & \textbf{State} \\
\begin{matrix} U_1 \\ U_2 \\ . \\ . \\ . \\ U_{M-1} \\ U_M \end{matrix} &
\begin{bmatrix} SINR_1, & CQI_1, & RSRQ_1 \\ SINR_2, & CQI_2, & RSRQ_2 \\ .\;\;. & .\;\;. & .\;\;. \\ .\;\;. & .\;\;. & .\;\;. \\ .\;\;. & .\;\;. & .\;\;. \\ SINR_{M-1}, & CQI_{M-1}, & RSRQ_{M-1} \\ SINR_M, & CQI_M, & RSRQ_M \end{bmatrix} &
\begin{bmatrix} s_1 \\ s_2 \\ . \\ . \\ . \\ s_{M-1} \\ s_M \end{bmatrix}
\end{array}$$

FIGURE 2. The structure of the input data

3. SIMULATION ENVIRONMENT

The KPI parameters in the input matrix are generated via Vienna LTE-A Simulator on MATLAB, which is a well-known downlink system level simulator for LTE/LTE-A networks [12]. In the simulations we employed eNodeBs with hexagonal geometry using 7 cells with one ring around the one in the middle, shown in Figure 3. We have assigned a total of 700 UEs with 100 UEs for each eNodeB and we used only the parameters of UEs belonging to the cell in the middle for the purpose of attaining more realistic KPIs with thorough interference effects. The radiating power of the healthy and outage cells were determined as 46 dBm and 0 dBm, respectively.

According to the simulation scenario, the power of the healthy cell degrades from 46 dBm to 0 dBm. To generate the training data, the three KPI parameters are recorded for both healthy and outage states. For testing procedure, the same simulations with UEs on different random locations but the eNodeBs in their original places are operated so that the KPI parameters are generated. The resulting KPI parameters are tested with the formerly trained Neural Network. The parameters of the simulations are given in Table 1. In the simulation environment, we planned an urban type environment with an inter-cellular distance of 500 meters. 20 transmission time interval (TTI) of simulation time was considered as suitable because it is sufficient for the radio access network parameters to settle down to their stable values.

TABLE 1. Simulation Parameters

Parameters	**Values**
Cellular Layout	7 eNodeBs
BS Tx Power for healthy cells	46 dBm
BS Tx Power for outage cell	0 dBm
Path Loss Model	TS36942 urban
Number of UEs per cell	100
UEs' mobility	Uniformly random distributed, random walk model with constant speed
Channel Bandwidth	5 MHz
Inter eNodeB Distance	500 m
Simulation Duration	20 TTI

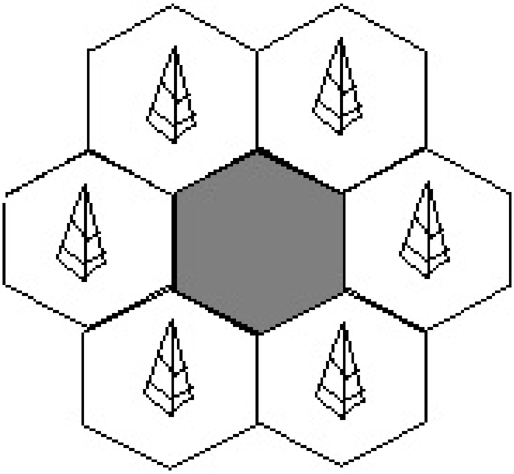

FIGURE 3. Hexagonal Cellular Structure with one ring around the center cell

4. RESULTS

Training process of the Neural Network starts with random initializations of the weights. For this reason the iterations may converge to local optima and may end with slight differences in terms of adjusted weights. Therefore the procedure of training the net, testing the data and computing the success rate is repeated 50 times so that an overall average success rate is reached. At the end of simulations the success rate of detecting an outage has come out to be 79.74%. Classification Performance of Neural Networks is also given in Table 2. In the Neural Network structure 10 neurons are employed and 10-fold cross validation is applied on the classification process. For comparison purposes, Logistic Regression and K-Means Algorithms were also applied. Binary Logistic Regression (LR) is one of the well-known pattern recognition methods used in binary classification problems. It is basically a regression process where the regression coefficients are computed by employing multi-dimensional training data within a least squares error approach and the output is generated by using the exponential operation on computed coefficients along with the data to be tested. The overall success rate for Logistic Regression was 78.73% and contingency table is given in Table 3. (True Positive (TP) Rate = 88.15%, True Negative (TN) Rate = 69.3%, False Positive (FP) Rate = 28.13% and False Negative (FN) Rate = 13.39%). On the other hand, K-Means algorithm which is an unsupervised clustering method, was also applied on the test data. Due to unsupervised nature of K-Means Algorithm, the overall success rate was limited to 66.8%.

TABLE 2. Classification Analysis of Neural Networks (Contingency Table)

	Real Outage Cases	**Real Healthy Cases**
Classified as outage	TP Rate = 87.61%	FP Rate = 28.13%
Classified as healthy	FN Rate = 13.39%	TN Rate = 71.87%

TABLE 3. Classification Analysis of Logistic Regression (Contingency Table)

	Real Outage Cases	**Real Healthy Cases**
Classified as outage	TP Rate = 88.15%	FP Rate = 30.7%
Classified as healthy	FN Rate = 11.85%	TN Rate = 69.3%

In cellular systems with dense deployment, the detection rates of the outages may further be improved by employing larger training data because as training sets increase there may be more information available to the classification algorithm [13]. Moreover employing more powerful machine learning mechanisms such as state-of-the-art deep learning architectures may also improve the detection performance.

5. CONCLUSION

In this study we have classified the eNodeBs into two categories as healthy and outage. We have applied artificial Neural Networks, a novel method for pattern recognition purposes, on the three KPI parameters (SINR, CQI and RSRQ) of the UEs reported periodically to the eNodeBs. Our proposed classification method has an outage prediction accuracy of 79.74% and success rate with Logistic Regression was computed as 78.73%. Having larger training datasets and employing more efficient methods like state-of-the-art deep learning architectures can further increase accuracy. Our study conducted Neural Network approaches on outage detection with cellular structures having eNodeBs. Therefore this study should be enhanced by employing other pattern recognition/classification methods such as Support Vector Machines, Hidden Markov Models and Deep Learning Structures along with ultra-dense multi-tier network structures (femto, micro, pico cells) that are likely to take place in future 5G systems.

REFERENCES

[1] Amirijoo, M & Jorguseski, Ljupco & Kürner, Thomas & Litjens, Remco & Eden, Michaela & Schmelz, Lars & Turke, U, Cell Outage Management in LTE Networks. *Proceedings of the 2009 6th International Symposium on Wireless Communication Systems*, ISWCS 09. (2009), 600-604. 10.1109/ ISWCS. 2009.5285232.

[2] 3rd Generation Partnership Project; Technical Specification Group Services and System Aspects; Telecommunications Management; Self-Organizing Networks (SON); Self-Healing Concepts and Requirements (Release 11), 3GPP TS 32.541, 2012-09, v11.0.0, 2012.

[3] Wang, W., Liao, Q. and Zhang, Q., COD: A cooperative cell outage detection architecture for self-organizing femtocell networks, *IEEE Trans. Wireless Commun.*, vol. 13, no. 11, , (Nov. 2014), pp. 6007–6014.

[4] De la Bandera, I., Barco, R., Munoz, P. and Serrano, I., Cell outage detection based on handover statistics, *IEEE Commun. Lett.,* vol. 19, no. 7, (Jul. 2015), pp. 1189–1192.

[5] Mueller, C., Kaschub, M., Blankenhorn, C. and Wanke, S., A cell outage detection algorithm using neighbor cell list reports, *Proc. Int. Workshop Self-Organizing Syst.*, (2008), pp. 218–229.

[6] Liao, Q., Wiczanowski, M. and Stanczak, S., Toward cell outage detection with composite hypothesis testing, *Proc. IEEE ICC*, Jun. 2012, pp. 4883–4887.

[7] Ma, Y., Peng, M., Xue, W. and Ji, X., A dynamic affinity propagation clustering algorithm for cell outage detection in self-healing networks, *Proc. IEEE WCNC*, (Apr. 2013), pp. 2266–2270.

[8] Khanafer, R. et al., Automated diagnosis for UMTS networks using Bayesian network approach, *IEEE Trans. Veh. Technol.,* vol. 57, no. 4, (Jul. 2008), pp. 2451–2461.

[9] Alias, M., Saxena, N. and Roy, A., Efficient Cell Outage Detection in 5G HetNets Using Hidden Markov Model, *IEEE Communications Letters*, vol. 20, no. 3, (March 2016), pp. 562-565.

[10] Onireti, O. *et al.*, A Cell Outage Management Framework for Dense Heterogeneous Networks, *IEEE Transactions on Vehicular Technology*, vol. 65, no. 4, (April 2016), pp. 2097-2113.

[11] Bodrog, L., Kajo, M., Kocsis S. and Schultz, B., A robust algorithm for anomaly detection in mobile networks, *2016 IEEE 27th Annual International Symposium on Personal, Indoor, and Mobile Radio Communications (PIMRC)*, Valencia, (2016), pp. 1-6.

[12] Ikuno, J. C., Wrulich, M. and Rupp, M., System Level Simulation of LTE Networks, *2010 IEEE 71st Vehicular Technology Conference*, Taipei, (2010), pp. 1-5.

[13] Cortes, C., Jackel, L. D., Solla, S. A., Vapnik, V., and Denker, J. S., Learning curves: Asymptotic values and rate of convergence, In Cowan, J. D., Tesauro, G., and Alspector, J., editors, Morgan Kaufmann Publishers Inc., *NIPS* volume 6, (1994), 327–334.

Current Address: HASAN TAHSİN OĞUZ: Ankara University Electrical and Electronics Engineering Department Gölbaşı ANKARA TURKEY
E-mail : htoguz@ankara.edu.tr
ORCID: https://orcid.org/0000-0002-8970-5511

Current Address: AYKUT KALAYCIOĞLU: Ankara University Electrical and Electronics Engineering Department Gölbaşı ANKARA TURKEY
E-mail : kalaycioglu@ankara.edu.tr
ORCID: https://orcid.org/0000-0001-8291-9958

Commun.Fac.Sci.Univ.Ank.Series A2-A3
Volume 60, Number 1, Pages 41-64(2018)
DOI: 10.1501/commua1-2_0000000110
ISSN 1303-6009 E-ISSN 2618-6462
http://communications.science.ankara.edu.tr/index.php?series=A2A3

COMPUTATIONAL BIFURCATION ANALYSIS TO FIND DYNAMIC TRANSITIONS OF THE CORTICOTROPH MODEL

SEVGİ ŞENGÜL AYAN AND AHMET KURT

ABSTRACT. The corticotroph model is a 7th order nonlinear differential equation system derived for representing the action potential dynamics of corticotrophs; one of the endocrine cells that is responsible for stress regulation. Here we use numerical continuation methods to perform bifurcation analysis since controlling bifurcations in the hormonal dynamics may bring some new insights in the treatment of stress related disorders. We study the bifurcation structure of the system as a function of the BK-channel dynamic parameters and the all maximal conductances. We identify the regions of bistability and bifurcations that shape the transitions between resting, bursting and spiking behaviors, and which lead to the appearance of bursting which is directly connected to stress regulation. Furthermore, we find that there are two routes to bursting, one is the experimentally observed BK-channel dynamics and the other is Ca^{2+} channel conductance only. Finally, we discuss how some of the described bifurcations affect dynamic behavior and can be tested experimentally.

1. INTRODUCTION

Systems of ordinary differential equations (ODEs) have a great impact on understanding the many biological systems, like electrically excitable cells ([1], [2]), growth dynamics [3] or chemical reaction networks [4]. Another approach for such systems is stochastic approach [5] but when it comes to numerical simulations of large nonlinear models and parameter estimation, ODE-based models offer a variety of analysis methods [6]. Another important property of ODE models for biological models are, we can observe very different dynamics for different sets of parameters such as stable/unstable equilibriums, limit cycles, periodic or chaotic orbits. A challenging part in developing and analyzing such models is to understand how parameters of the model affect features of its such dynamics. Numerical solution of

---

Received by the editors: June 08, 2018; Accepted: July 24, 2018.
Key word and phrases: Dynamical System, bifurcation analysis, Corticotroph model, bursting and spiking oscillations.

these models with hand tuning of parameters is a first approach to predict the system's behavior and effects on solutions [7]. But trusting the modeler's intuition by manual inspection of the equations is not a suitable approach for non–trivial systems. At this point we need a more powerful approach to see the specific behavior, and how this depends on parameter values.

Excitable electric activity is observed to many biological systems; such as some isolated or coupled neurons, hormone secretion, muscle contraction or heart cells. This activity plays an essential role for the function of the cell as well as for its communication with neighboring cells. From a dynamical system point of view, a slight perturbation of the single stable stationary state by changing related parameter would lead to a large and long-lasting shift away from stationary point before the system asymptotically returning to equilibrium. Performing numerical continuation methods to perform bifurcation analysis is often a powerful way to analyses the properties of such systems, since it predicts what kind of behavior occurs where in parameter space ([7], [8]). Bifurcation analysis start with computing all equilibrium and periodic solutions of the system along with information about the stability of these solutions. Bifurcation diagrams are created later from the curves of equilibrium solutions as one of the parameters is varied while all other parameters are held fixed. To generate an entire family of bifurcation diagrams, this procedure can be repeated for all important parameters as a variable.

In this paper we focus on the analysis of CRH/AVP bursting in corticotroph cells of the pituitary using the mathematical model that author defined in the previous work [2]. These cells are responsible for the neuroendocrine response to stress as an integral component of the hypothalamic–pituitary–adrenal (HPA) axis. Corticotrophs display mostly single spike activity under basal conditions that transition to complex bursting behaviors upon stimulation by the CRH and AVP, however the underlying mechanisms controlling bursting in terms of dynamical system viewpoint are unknown. Similar bursting behavior that we describe for corticotrophs is known to occur in a variety of other cell types as well. For instance, Morris and Lecar [9] modeled the complex firing patterns in barnacle giant muscle fibers, for pacemaker neurons burst patterns are shown by Pant and Kim [10], bursting patterns in discharging cold fibers of the cat are investigated by Braun et al.

[11]. But biophysical mechanism underlying the bursting behavior vary significantly from cell type to cell type.

To this aim, we use mathematical modeling, numerical simulations and dynamical systems theory approaches to investigate the dynamic behavior of the corticotroph system. Parameter regimes for spiking and bursting activity are not investigated before, a detailed mathematical analysis of the dynamical regimes of the model has not performed yet. We study the bifurcation structure of the system as a function of conductances and parameters responsible for bursting. We identify the bifurcations that shape the transitions between resting, bursting and spiking behaviors which lead to the appearance of bursting after the stimulation with CRH. Insights gained from these analyses helped us to understand how the activity changes arise and whether there is other parameter set that can cause bursting for corticotrophs. These insights will provide us measurable results with experiments. Due to the complexity of the model, a great deal of extra insight can be gained by analyzing how some of the many other parameters shape the dynamical landscape of the model. Traditionally this has been used to isolate computationally important variables, responsible for bursting, given the difficulty of teasing apart the system experimentally.

2. THE CORTICOTROPH MODEL

As the basis for our bifurcation analysis, we will use the following model suggested by the author without the noise term [2];

$$C_m \frac{dV}{dt} = -\left(I_{Ca} + I_{K-dr} + I_{BK-near} + I_{BK-far} + I_{K-ir} + I_{NS}\right) \tag{2.1}$$

$$I_{Ca}(V) = g_{Ca} m_\infty(V)(V - V_{Ca}) \tag{2.2}$$

$$I_{K-dr}(V) = g_K n(V - V_K) \tag{2.3}$$

$$I_{K-ir}(V) = g_{K-ir} r_\infty(V)(V - V_K) \tag{2.4}$$

$$I_{BK-far}(V, c) = g_{BK-far} bk_f (V - V_K) \tag{2.5}$$

$$I_{BK-near}(V, c_{dom}) \; = \; g_{BK-near} bk_n (V - V_K) \tag{2.6}$$

$$I_{NS}(V) = g_{NS}(V - V_{NS}) \tag{2.7}$$

$$\frac{dn}{dt} = \frac{n_\infty(V) - n}{\tau_n} \tag{2.8}$$

$$x_\infty(V) = \frac{1}{1 + e^{\left(\frac{v_x - V}{s_x}\right)}}, \qquad x = n, m, r \tag{2.9}$$

$$\frac{dbk_n}{dt} = \frac{bk_{n\,\infty}(V, c_{DOM}) - bk_n}{\tau_{bk_n}} \tag{2.10}$$

$$\frac{dbk_f}{dt} = \frac{bk_{f\,\infty}(V, c) - bk_f}{\tau_{bk_f}} \tag{2.11}$$

$$bk_{n_\infty}(V, c_{DOM}) = \frac{1}{1 + \exp\frac{-\left(V - V_{bk-near}(c_{DOM})\right)}{k_{bk}}} \tag{2.12}$$

$$bk_{f_\infty}(V, c) = \frac{1}{1 + \exp\frac{-\left(V - V_{bk-far}(c)\right)}{k_{bk}}} \tag{2.13}$$

$$V_{BK-near}(c_{DOM}) = V_{BK_0} - k_{shift} \ln \frac{c_{DOM}}{k_{Ca_{BK-near}}} \tag{2.14}$$

$$V_{BK-far}(c) = V_{BK_0} - k_{shift} \ln \frac{c}{k_{Ca_{BK-far}}} \tag{2.15}$$

$$c_{DOM} = -A I_{Ca-L}(V) \tag{2.16}$$

$$\frac{dc}{dt} = -f(\alpha I_{Ca} + k_c c) \tag{2.17}$$

There are six ionic currents in the model, I_{CaL} is the high voltage activated L-type Ca^{2+} current, I_{Kdr} is the rapidly activated delayed rectifier K^+ current, IBK-near is the large-conductance, voltage and Ca^{2+}-activated K^+ channels located near Ca^{2+} channels and respond to Ca^{2+} in microdomains. $I_{BK\text{-}far}$ channels are located away from Ca^{2+} channels and respond to the mean cytosolic Ca^{2+} concentration. I_{Kir} is the inward rectifier K^+ current that activates under hyperpolarization. Also, I_{ns} in the model is a current produced by non-selective-cation channels. n is the gating variable for the activation of I_{Kdr} current. $x_\infty(V)$ shows the steady-state functions.

The gating variables for the near and far populations of BK channels with the equilibrium functions are shown with the bk_n and bk_f equations. Here Ca_{dom} is the free Ca^{2+} concentration in a microdomain and c is the mean free cytosolic Ca^{2+} concentration.

TABLE 1. Parameter values

Parameters	Values	Parameter	Value
g_{Ca-L}	1.8 nS (basal), 2.2 nS (CRH)	$k_{Ca_{BK-near}}$	18 μM (basal), 6 μM (CRH)
g_{NS}	0.1 nS (basal), 0.2 nS (AVP)	$k_{Ca_{BK-far}}$	0.6 μM
g_K	8.2 nS	k_{bk}	1 mV
g_{K-ir}	1 nS	s_m	10
$g_{BK-near}$	2 nS	s_n	10
g_{BK-far}	1 nS	s_r	-1
V_{Ca}	60 mV	V_{BK_0}	0.1 mV
V_{NS}	-10 mV	k_{shift}	20
V_K	-75 mV	A	0.15
v_r	-60 mV	k_c	0.12 μM

v_{m}	-20 mV	f	0.01
v_{n}	-5 mV	α	0.0015
$\tau_{\mathrm{bk_n}}$	20 ms (basal), 4 ms (CRH)	σ_{N}	5 pA
$\tau_{\mathrm{bk_f}}$	4 ms	C_{m}	6 nF

Bifurcation and continuation analysis was conducted in PyDSTool, PYTHON based tool for simulating and analyzing dynamical systems. One and two-parameter bifurcation diagrams were constructed using AUTO within PyDSTool [12].

3. RESULTS

We can apply numerical continuation to each rate constants and dynamic parameters for currents to determine which oscillations appear or disappear and how these transitions between a stable and unstable steady state happens ([13], [14], [15], [16], [17]). But experimentally making these changes mostly impossible. In the original paper [2], authors saw that making the BK-near channels similar to BK-far channels by reducing the time constant and right-shifting its activation curve was sufficient to convert spiking to bursting without the need to make any other changes but how this transition happens is unknown. Also, with the dynamic clamp study, it has been shown that BK-near channel conductance induces bursting in pituitary cells [18]. Given the difficulty of teasing apart the system experimentally, understanding the dynamic mechanisms behind these transitions and responsible parameters are important because this will give us the reason for the changes after stress hormone regulation. These shifts in excitability is regulated by two hormones CRH and AVP that cause corticotrophs to respond differently to various stressors. Figure 1 shows an example of the temporal variations of the voltage V as obtained by simulating the cell model under conditions where it exhibits a characteristic spiking (Fig. 1a) and bursting (Fig. 1b) dynamics after the stimulation with CRH/AVP. Understanding the dynamic mechanisms under these shifts between resting, spiking and bursting is important because these results will give us applicable predictions on stress regulation. Therefore, we begin by investigating the changes between spiking and bursting behavior for the experimentally observed parameters in section 3.1 first and then we will analyze the transitions between resting, spiking and possible bursting states in section 3.2 with all conductances using bifurcation analysis.

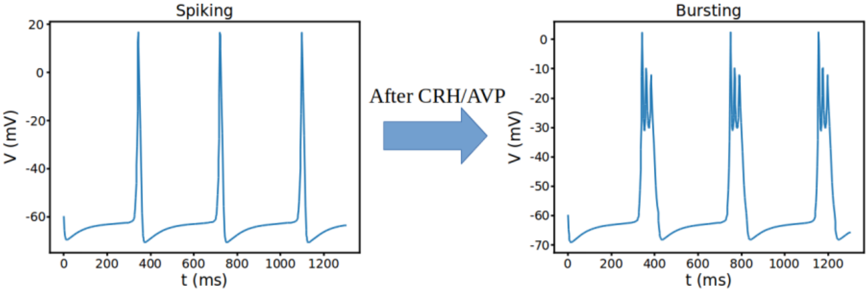

FIGURE 1. Spiking and bursting patterns of the corticotroph model respectively. Parameter differences are as follows: Spiking ($\tau_{bk_n} = 20$, $g_{NS} = 0.1$, $g_{Ca} = 1.8$, $k_{Ca_{BK-near}} = 18$), Bursting ($\tau_{bk_n} = 4$, $g_{NS} = 0.2$, $g_{Ca} = 2.2$, $k_{Ca_{BK-near}} = 6$).

3.1 Bifurcation analysis for bursting parameters $k_{Ca_{BK-near}}$ and τ_{bk_n}

In order to investigate the contribution of BK-channel dynamics to the overall dynamics and characterize bifurcation types in the model, BK-far and BK-near conductances ($g_{BK-near}$ and g_{BK-far}) are investigated first but no bifurcation is observed. That means that BK channel conductances are not responsible for the bursting but the parameters for the channel dynamics are. Moreover, two important parameters responsible for bursting are: time constant of the BK-near channel τ_{bk_n} and activation parameter $k_{Ca_{BK-near}}$ values, during spiking and bursting regime are examined separately.

3.1.1 Bifurcation for the BK-channel activation curve parameter '$k_{Ca_{BK-near}}$' during spiking regime

We start our analysis of the bifurcation structure for spiking regime, the parameter values used here are: $\tau_{bk_n} = 20$, $g_{NS} = 0.1$, $g_{Ca} = 1.8$. Fig. 2 shows the bifurcation diagram of the spiking regime (a) and some voltage traces with different values of $k_{Ca_{BK-near}}$. There are two Hopf bifurcations, two saddle-node bifurcations and one saddle node on periodic orbit bifurcations as a result of numerical continuation with respect to $k_{Ca_{BK-near}}$ parameters. For the small values of $k_{Ca_{BK-near}}$ parameter, the bottom branch of the steady states are stable nodes and the stability lost with the first saddle-bode bifurcation (SN1) at $k_{Ca_{BK-near}} = 0.039949$ leading to a branch of saddles which again turns around at another saddle-node bifurcation (SN2) $k_{Ca_{BK-near}} = 0.03$, before regaining stability again via a subcritical Hopf bifurcation. Subthreshold oscillations (Fig. 2b blue dashed line) start at subcritical Hopf point H1 at $k_{Ca_{BK-near}} = 0.39944$ where unstable steady states turn into stable ones with the rise of unstable periodic branch and ends with supercritical Hopf bifurcation point H2 at $k_{Ca_{BK-near}} = 0.1434$ where these stable steady states lost their stability. Here at saddle-node bifurcation of periodic solutions (SNP) at $k_{Ca_{BK-near}} = 0.179$, unstable periodic orbits also become stable ones. Here the branch of stable periodic spiking solutions emanating from the H2 grows in amplitude and period with increasing $k_{Ca_{BK-near}}$ parameter. Subthreshold oscillations grow in amplitude and become regular spiking that can be seen in Fig. 2b (orange line). This suggests that for the slow activation of bk_{near} channels ($\tau_{bk_n} = 20$), shifting activation curve right or left by changing $k_{Ca_{BK-near}}$ does not have any physiological role as promoting bursting, instead it only increases the frequency of spiking.

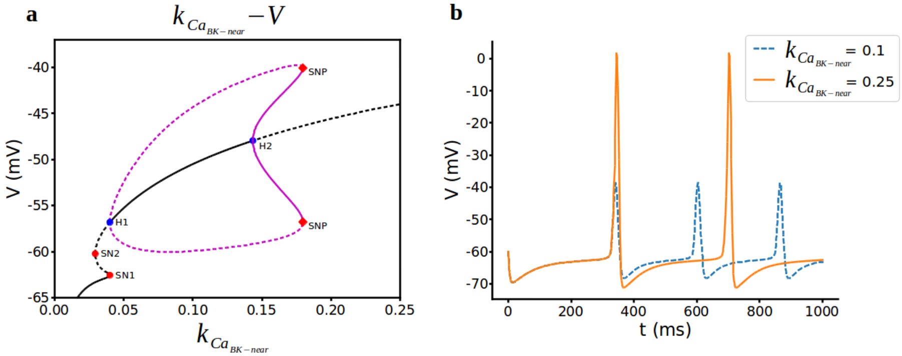

FIGURE 2. Bifurcation analysis for BK_{near}-activation curve parameter $k_{Ca_{BK-near}}$ during spiking regime. a) Bifurcation diagram with $k_{Ca_{BK-near}}$ as the bifurcation parameter. Stable nodes (black line), unstable nodes or saddles (black dashed line), stable periodic orbit (magenta line), unstable periodic orbit (magenta dashed line), bifurcation points (red and blue dots). SN1 saddle node bifurcation 1, SN2 saddle node bifurcation 2, H1 subcritical hopf bifurcation, H2 supercritical hopf bifurcation, SNP saddle-node on periodics bifurcation. b) Representative traces of voltage at different values of $k_{Ca_{BK-near}}$.

3.1.2 Bursting regime and bifurcation for the BK-channel activation curve parameter '$k_{Ca_{BK-near}}$'

The bifurcation diagram, when $\tau_{bk_n} = 4$ and using $k_{Ca_{BK-near}}$ again as the bifurcation parameter, is qualitatively different than when $\tau_{bk_n} = 20$ (Fig. 3). Saddle-node bifurcations appear the same way and H1 point still rise a subcritical hopf bifurcation but there is a homoclinic bifurcation (HC) now just after the hopf point (Fig. 3b). Oscillations starting here ends with hyperpolarized resting state and with increasing $k_{Ca_{BK-near}}$ parameter means that shifting the half activation of BK-near channel to the right makes hyperpolarized state rises to higher voltages (Fig. 3c). At H2, supercritical hopf bifurcation starts with periodic branches open to right now and stable periodic branches turn to unstable periodic branches at period doubling bifurcation (PD) (Fig. 3a). There is a fast spiking between this area (Fig. 3c). For further increasing $k_{Ca_{BK-near}}$, spike doubling behaviour transitions to bursting as a result of CRH effect as in original model (Fig. 3d). Firstly, number of spikes per burst decreases (Fig. 3e,f) and then the bursting dynamics ends in a different type of process, referred to as a homoclinic bifurcation. Finally, the periodic solutions disappear via a homoclinic bifurcation (HC) at $k_{Ca_{BK-near}} = 10.612$ which the period is infinitely large. In the interval of coexisting stable solutions, the stable manifold of the saddle point defines the boundary of the basins of attraction for the stable node and limit cycle solutions. The basin of attraction for a stable solution represents the set of initial conditions from which trajectories asymptotically approach the solution. When the limit cycle for increasing values of $k_{Ca_{BK-near}}$ hits its basin of attraction, another limit cycle appears through period doubling bifurcation. The characteristic slowing down of the spiking dynamics as the system approaches the end of the bursting phase observed as in Fig. 3e. The coordinates ($k_{Ca_{BK-near}}$, V) of the bifurcation points are as follows: H1 (0.032, -58.57), SN1 (0.04, -62.5), SN2 (0.03, -60.2), HC1 (0.03, [-56.84, -61,75]), H2 (1.16, -32.26), PD (5.33, [-7.07, -43.72]), HC2 (10.6, [-3.19, -36.3]). As can be seen here, bursting arises due to the rapid rate of BK channel activation since we decrease the τ_{bk_n} from 20 to 4 and our bifurcation analysis shows that this transition is happening with the period doubling bifurcation.

3.1.3 Varying $k_{Ca_{BK-near}}$ and τ_{bk_n} simultaneously: codimension-2 analysis

As stated while $k_{Ca_{BK-near}}$ can induce bursting itself, τ_{bk_n} may not be able to induce bursting by itself. The natural cause of action is thus to investigate what happens as these 2 parameters are varied simultaneously. Due to the complexity of the system, an analytic codimension analysis is impossible. Therefore, a numerical codimension 2 analysis will be enough to see the dynamics once we change both parameters simultaneously. If we vary two parameters, the curves of Hopf bifurcation is given below. We can see there is no oscillatory region between the Hopf points. Bursting regime stays after H2 point and Hopf points getting away from each other with increasing $k_{Ca_{BK-near}}$. In Fig. 4 we can see clearly that time dependency of the activation of BK channel alone cannot induce bursting and Hopf bifurcation is not responsible for characterizing the route to bursting.

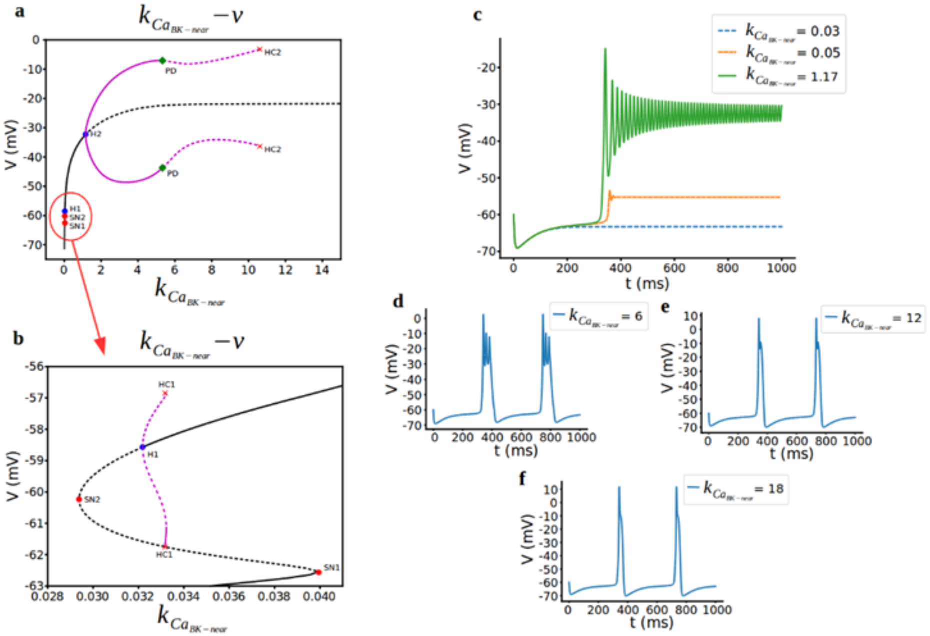

FIGURE 3. Bifurcation analysis for $\mathrm{BK_{near}}$-activation curve parameter $\mathrm{k_{Ca_{BK-near}}}$ during bursting regime. a,b) Bifurcation diagram with $\mathrm{k_{Ca_{BK-near}}}$ as the bifurcation parameter. Stable nodes (black line), unstable nodes or saddles (black dashed line), stable periodic orbit (magenta line), unstable periodic orbit (magenta dashed line), bifurcation points (red and blue dots). SN1 saddle node bifurcation 1, SN2 saddle node bifurcation 2, H1 subcritical hopf bifurcation, H2 supercritical hopf bifurcation, HC1 homoclinic bifurcation 1, HC2 homoclinic bifurcation 2 and PD period doubling bifurcation. c,d,e,f) Representative traces of voltage at different values of $\mathrm{k_{Ca_{BK-near}}}$.

3.2 Dependence of model cell behavior on conductances

3.2.1 Non-selective cation conductance g_{ns}

Duncan et al. [2] showed that increasing the non-selective cation channel conductance (g_{ns}) only increases spike frequency as a result of AHP effect. Here we examine the bifurcation diagram with respect to g_{ns} to see how cell is differing stabilities according to changing non-selective cation current. Also, it is known that Ca^{2+} dependent non-selective cation channel may induce bursting in different cells ([19], [20]). The bifurcation diagram using g_{ns} as the initial bifurcation parameter is formed an s-shaped curve of steady states and a curve of periodic orbits (Fig. 5a).

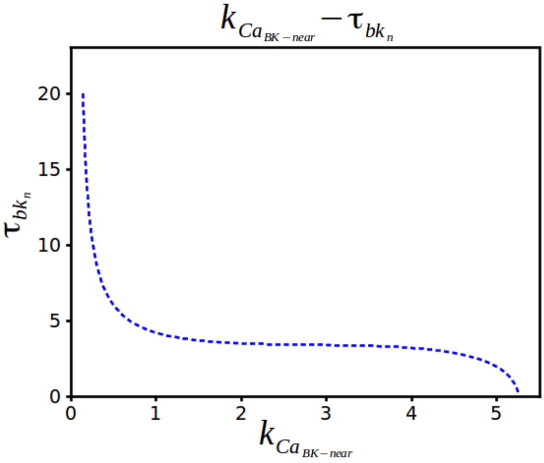

FIGURE 4. Two-parameter bifurcation diagram for τ_{bk_n} *vs.* $k_{Ca_{BK-near}}$.

The lower branch of the s-curve consists of stable nodes which correspond to the hyperpolarized resting state of the cell. Stability is lost via saddle-node bifurcation at (g_{ns}, V) = (0.099, -62.652), and gives rise to a branch of saddles, which forms the middle and part of the upper branches of the s-curve. From the Fig. 5a, the periodic solutions appearing for low g_{ns} via a saddle-node on an invariant circle (SNIC) bifurcation and cell shows regular spiking here (Fig. 5b orange line). The saddle-node bifurcation of equilibrium solutions corresponding to this value of g_{ns} is that saddle-node point. This branch of saddles is regaining stability at the supercritical hopf bifurcation at (g_{ns}, V) = (1.047, -19.97). Here, periodic branches disappear and for increasing g_{ns} there remains a branch of stable nodes, corresponding to a depolarized resting state at around -20mV (Fig. 5c orange dashed line).

Indeed, increasing the maximal conductance of non-selective cation channel only increases frequency first (Fig. 5c blue line), then regular spikes turns to subthreshold oscillations and does not induce bursting and cell is either hyperpolarized or depolarized state otherwise. As a result, increasing the non-selective cation conductance did not initiate that transition to bursting for corticotroph cells, but increased burst frequency and decrease amplitude.

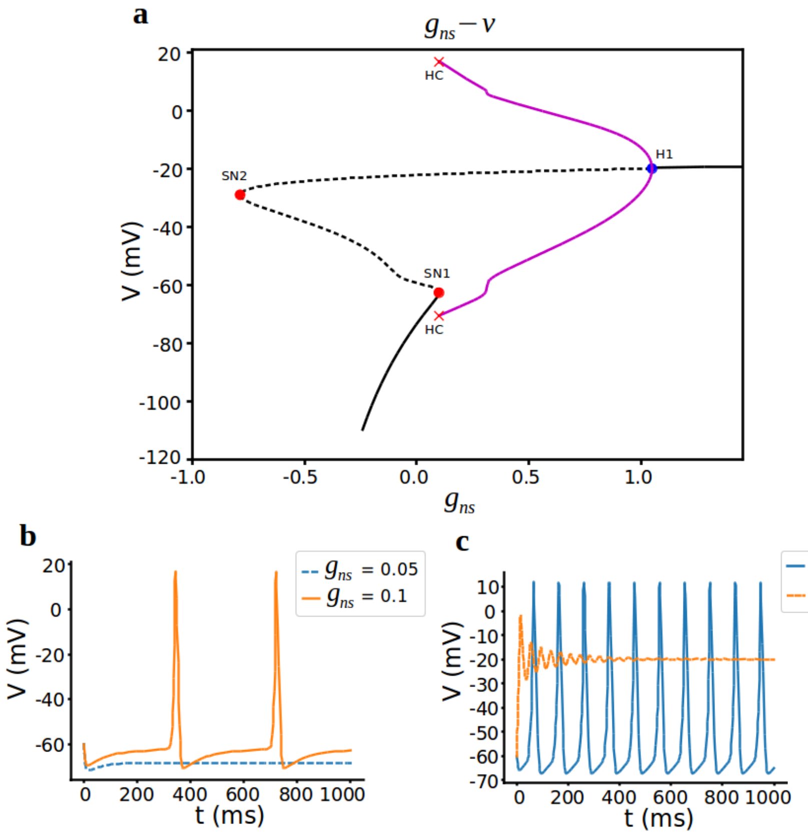

FIGURE 5. Bifurcation analysis for non-selective cation conductance g_{ns}. a) Bifurcation diagram with g_{ns} as the bifurcation parameter. Stable nodes (black line), unstable nodes or saddles (black dashed line), stable periodic orbit (magenta line), unstable periodic orbit (magenta dashed line), bifurcation points (red and blue dots). SN1 saddle node bifurcation 1, SN2 saddle node bifurcation 2, H1 supercritical hopf bifurcation, HC homoclinic bifurcation. b,c) Representative traces of voltage at different values of g_{ns}.

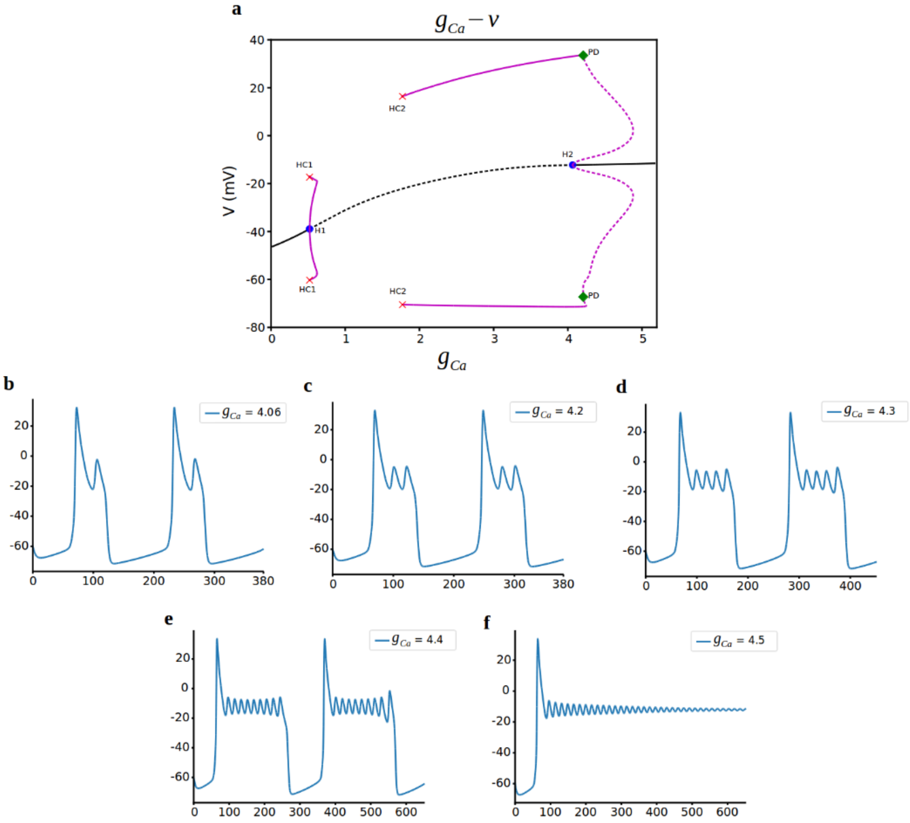

FIGURE 6. Bifurcation analysis for L-type Ca current conductance g_{Ca}. a) Bifurcation diagram with g_{Ca} as the bifurcation parameter. Stable nodes (black line), unstable nodes or saddles (black dashed line), stable periodic orbit (magenta line), unstable periodic orbit (magenta dashed line), bifurcation points (red and blue dots). H1 supercritical hopf bifurcation, H2 subcritical hopf bifurcation, HC1 homoclinic bifurcation 1, HC2 homoclinic bifurcation 2, PD period doubling bifurcation. b,c,d,e,f) Representative traces of voltage at different values of g_{Ca}.

3.2.2 L-Type Ca^{2+}-current conductance g_{Ca}

The possibility of other ionic current to generate the bursting activity is examined by changing the L-type Ca^{2+} current conductance g_{Ca}. Fig. 6 shows the one-parameter bifurcation diagram where g_{Ca} is the bifurcation parameter. For the lower values of g_{Ca}, only one stable equilibrium point corresponding to the resting potential exists. When g_{Ca} is increased to 0.519, stability is lost via supercritical hopf bifurcation (H1) and stable periodic orbits decreases the hyperpolarized resting state with increasing g_{Ca}. Spiking starts with a creation of periodic orbits at homoclinic bifurcation (HC2) at $g_{Ca} = 1.77$ before regaining stability at the subcritical hopf bifurcation (H2) at $g_{Ca} = 4.06$ and switch spiking to bursting activity at this point. Bursting due to the Ca^{2+} channel was the unexpected and unseen results from the experiments. Our bifurcation analysis revealed another link to bursting for corticotroph cells that can be tested experimentally. Also, we observe another nice dynamic here. A period doubling bifurcation is associated with the loss of stability of these periodic solutions. In addition, we observe spike adding cascade at this point. As the bifurcation parameter g_{Ca} increase, the number of spikes per burst grows incrementally until bursting transforms into depolarized state (Fig. 6bcdef). For increasing g_{Ca} there remains a branch of stable nodes, corresponding to a depolarized resting state of around -10mV. The g_{Ca} values of the bifurcation points are as follows: H1 (0.519), HC1 (0.52), HC2 (1.77), H2 (4.065), PD (4.21).

Here when we look at the voltage traces, spiking starts at the homoclinic point around $g_{Ca} = 1.8$, and before that it is in hyperpolarized state around -65mV. The periodic branches that starts from H1 only decreases the resting state from -40mV to -65mV.

3.2.3 Delayed-rectifier potassium conductance g_K

The potential role of delayed rectifier K^+ channels in electrical activity was examined in various pituitary cells. In GH_3 cells, inhibition of this channel increases the duration of the AP [21] and the amplitude of the spontaneous [Ca^{2+}] transients [22] but in frog melanotrophs, the delayed rectifier K^+ conductance, leads to inhibition of electrical activity [23]. In rat lactotrophs, on the other hand, does not alter the pattern of AP firing [21]. For the corticotrophs, we examine here with the bifurcation analysis using g_K as the initial bifurcation parameter with different steady states and a curve of periodic orbits. When we look at the z-shaped curve in Fig. 7a, the lower values of g_K consists of stable nodes which correspond to the depolarized resting state of the cell. Stability is lost via a subcritical hopf bifurcation (H3) at (g_K, V) = (4.512, -12.810) and cell starts to spike at this point (Fig. 7c). Unstable periodic orbits of subcritical hopf bifurcation gains stability with bautin bifurcation also known as degenerate hopf bifurcation at B1 point that corresponds to saddle-node bifurcation of periodic orbits (Fig. 7b)

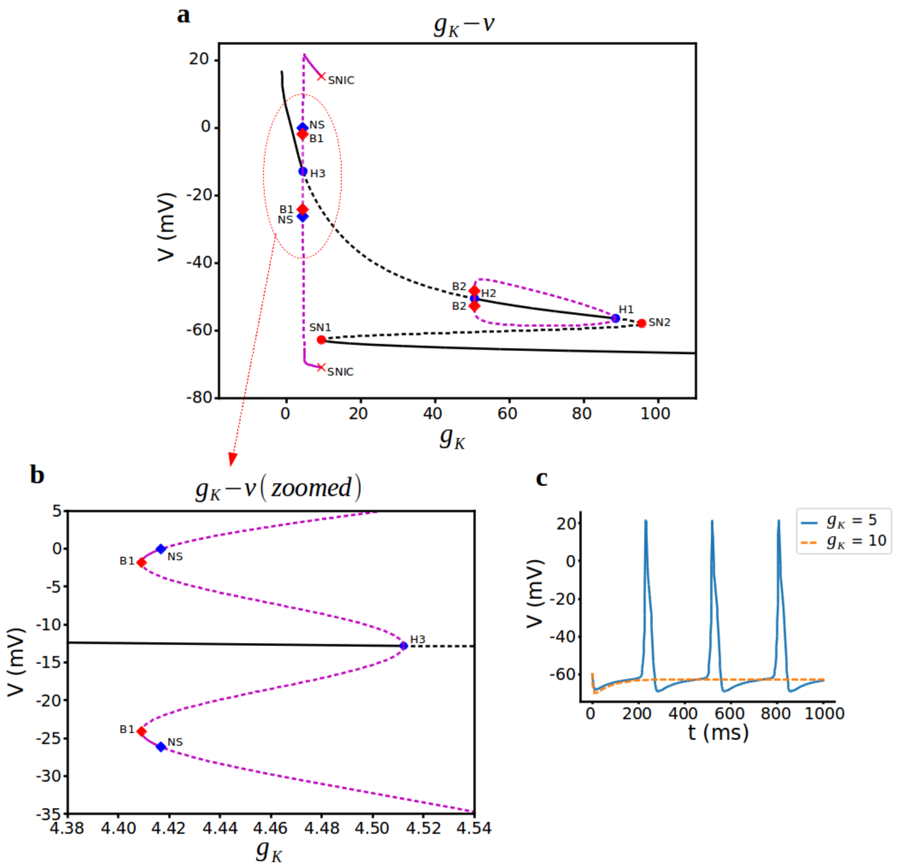

Figure 7: Bifurcation analysis for delayed rectifier K^+ current conductance g_K. a) Bifurcation diagram with g_K as the bifurcation parameter. Stable nodes (black line), unstable nodes or saddles (black dashed line), stable periodic orbit (magenta line), unstable periodic orbit (magenta dashed line), bifurcation points (red and blue dots). SN1 saddle node bifurcation 1, SN2 saddle node bifurcation 2, H1 subcritical hopf bifurcation 1, H2 supercritical hopf bifurcation 2, H3 subcritical hopf bifurcation 3, HC1 homoclinic bifurcation 1, HC2

homoclinic bifurcation 2, B1 Bautin bifurcation 1, B2 Bautin bifurcation 2, NS Neimark-Sacker bifurcation. b,c) Representative traces of voltage at different values of g_K.

In neural networks, bursting can be observed near bautin bifurcation [24] but in our system parameter region is small and this branch of stable orbits lost stability around at another bifurcation point, neimark-sacker bifurcation just after B1. For increasing g_K, there remains a branch of stable nodes corresponding to a spiking state until it vanishes with SNIC bifurcation at around $g_K = 9.455$. From the Fig. 7a, the periodic solutions disappearing via a saddle-node on an invariant circle (SNIC) bifurcation. The saddle-node bifurcation of equilibrium solutions corresponding to this value of g_K is that saddle-node point and cell goes in to hyperpolarized state after this point (Fig. 7c orange dashed line).

The z-shaped curve of steady-states create different periodic orbits here. The lower branch of the z-curve consists of stable nodes which correspond to the hyperpolarized resting state of the cell and middle unstable steady states turns to stable ones with the creation of unstable periodic orbits with 2 more hopf bifurcations, with one supercritical and the other is subcritical ones. Stable periodic orbits here lost their stability with another bautin bifurcation at B2 just after H2 point. Here again parameter region is so small between H2 and B2 and K^+ conductance values are so big for real cell. As a result, cell stays in hyperpolarized state in that region.

3.2.4 Inward-rectifier Potassium conductance g_{K-ir}

To complete the full bifurcation analysis in terms of the conductances, lastly, we change inward-rectifier potassium current conductance g_{K-ir} while others are intact. We know that K_{ir} channels play important roles in the control of resting membrane potential and inhibition of spontaneous electrical activity in pituitary cells [25]. The bifurcation diagram, using g_{K-ir} as the bifurcation parameter, is shown in Fig. 8a. The bottom branch of this curve consists of stable nodes, representing the hyperpolarized resting state. There is a saddle-node bifurcation at $g_{K-ir} = 0.694$ and regular spiking occurs before this point (Fig. 8b). For further increasing g_{K-ir}, firstly spiking slows down (Fig. 8c blue line) and cell turns into hyperpolarized resting state (Fig. 8c orange dashed line) means that it does not have enough Ca^{2+} to fire the action potential anymore. As we can see here, inward rectifier K^{+} channel does not promote bursting for corticotroph cells instead decrease in frequency of spiking and spiking to resting state transfer can be achieved with $K-ir$ channel.

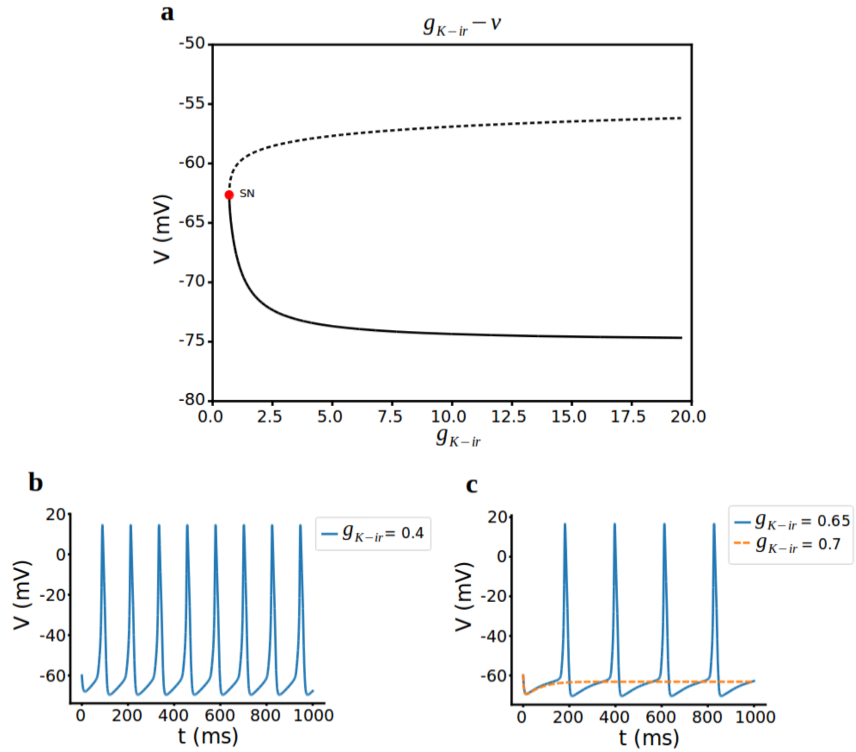

FIGURE 8. Bifurcation analysis for inward rectifier K^{+} current conductance g_{K-ir}. a) Bifurcation diagram with g_{K-ir} as the bifurcation parameter. Stable nodes (black line), unstable nodes or saddles (black dashed line), SN saddle node bifurcation. b,c) Representative traces of voltage at different values of g_{K-ir}.

4. DISCUSSION

4.1 Spiking Dynamics

The corticotroph model that the author defined in the previous work is used for the numerical bifurcation analysis to understand the dynamics under the transition between resting, spiking and bursting behavior. We show that corticotroph cells turn from silent phase to spiking phase with different bifurcation structures with the dynamic parameters of BK-channel dynamics ($k_{Ca_{BK-near}}$) that is experimentally observed before and conductances. As $k_{Ca_{BK-near}}$ is increased subthreshold oscillations emerge in the model at subcritical Hopf point. Subthreshold oscillations grow in amplitude and become regular spiking through saddle-node bifurcation of periodic solutions bifurcation. We observe that cell does not turn back to resting with the activation parameter of BK-channels.

The analysis shows that increasing g_{ns}, g_K and g_{K-ir} channel conductances shifts cell from resting to spiking through hopf bifurcations and rheobases are formed from saddle-node bifurcations. Here while increasing g_{ns} turns the cell into depolarized state, increasing g_K and g_{K-ir} conductances shift the cell into hyperpolarized state. As a result of our bifurcation analysis with L-type Ca^{2+} current conductance g_{Ca}, spiking starts with a creation of periodic orbits at homoclinic bifurcation, not hopf bifurcation as the other conductances. But the most important result was this spiking phase does not turn to resting instead we observe bursting behavior as explained in 4.2.

4.2 Bursting Dynamics

Given the importance of bursting activity in excitable cells, it is important to identify the key mechanisms underlying it. Experimental findings have shown that the intrinsic bursting of corticotroph cells is driven by BK- channels. But what kind of dynamic changes happens during the bursting was unknown. In this study we observed that BK channel conductances does not promote any dynamic changes for the cell instead shifting activation curve by $k_{Ca_{BK-near}}$ parameter was responsible together with activation time parameter τ_{bk_n} when BK-near channel dynamics was fast. During the slow activation of BK-near channels ($\tau_{bk_n} = 20$), shifting activation curve right or left by changing $k_{Ca_{BK-near}}$ does not have any physiological role as promoting bursting, instead it only increases the frequency of spiking.

As can be seen here, first bursting arises due to the rapid rate of BK channel activation since we decrease the τ_{bk_n} from 20 to 4 and transition is happening with the period doubling bifurcation and ends with homoclinic bifurcation. So, in our system the Hopf bifurcation is not relevant for characterizing the route to bursting but period doubling and homoclinic bifurcations are. Period-doubling bifurcation to chaos were discovered in spontaneous firings of Onchidium pacemaker neurons [26] before. In our system, the actual route depends on the relative location of the full-system's fixed point with respect to a homoclinic bifurcation. Stress regulation due to BK-channel is also observed experimentally [2] and in our study, we showed how this transition happens. But unexpected result is observed with L-type Ca^{2+} current. Hopf bifurcation that turns cell into spiking for other conductances in the model, for increasing g_{Ca} turns the cell into bursting phase this time. The bifurcation analysis conducted here revealed another link to stress regulation through Ca^{2+} channel alone and this can give us an experimentally tested prediction from the model [27,28] and computational analysis.

5. CONCLUSION

Bifurcation analysis with numerical continuation algorithm is applied to the considered model in order to examine its dynamical states. Characterizing the bifurcation structure for BK-channel parameters and conductances in corticotroph model to investigate the spiking and bursting regime in the system provides insight about the parameter dependence of the model dynamics. We have identified various routes from resting to spiking to bursting including Hopf bifurcations, SNIC or homoclinic bifurcations, period doubling and spike adding cascades. Also, our work shows that dynamical systems theory provides an efficient tool for examination of self-regulation of a full model of the neuroendocrine system. The results of our computational investigations may be used as a lead for designing experiments.

References

[1] Hodgkin, A. L., Huxley, A. F., “A quantitative description of membrane current and its application to conduction and excitation in nerve”, Journal of Physiology, 117(4) (1952) 500–544.

[2] Duncan, P. J., Sengul, S., Tabak, J., Ruth, P., Bertram, R., Shipston, M. J., “Large conductance Ca2+-activated K+ channels (BK) promote secretagogue-induced transition from spiking to bursting in murine anterior pituitary corticotrophs”, Journal of Physiology, 593(5) (2015) 1197–1211.

[3] Murphy, H., Jaafari, H., Dobrovolny, H. M., “Differences in predictions of ODE models of tumor growth: a cautionary example”, BMC Cancer, 16 (2016) 163.

[4] Mary Celin Sharmila, D., Praveen, T., Rajendran, L., “Mathematical Modeling and Analysis of Nonlinear Enzyme Catalyzed Reaction Processes”, Journal of Theoretical Chemistry, (2013) 2013:7.

[5] Schaff, J. C., Gao, F., Li, Y., Novak, I. L., Slepchenko, B. M., “Numerical Approach to Spatial Deterministic-Stochastic Models Arising in Cell Biology”, PLoS Comput Biol., 12(12) (2016) e1005236.

[6] Rinzel, J., A Formal Classification of Bursting Mechanisms in Excitable Systems, Springer Berlin Heidelberg, 1987.

[7] Sherman, A., “Dynamical systems theory in physiology”, The Journal of General Physiology, 138(1) (2011) 13–19.

[8] Strogatz, S. H., Nonlinear Dynamics and Chaos, Addison-Wesley Publishing Company, 2001.

[9] Morris, C., Lecar, H., “Voltage oscillations in the barnacle giant muscle fiber”, Biophys J., 35(1) (1981) 193–213.

[10] Plant, R. E., Kim, M., “Mathematical descriptions of a bursting pacemaker neuron by a modification of the Hodgkin-Huxley equations”, Biophys. J., 16(3) (1976) 227–244.

[11] Braun, H. A., Bade, H., Hensel, H., “Static and dynamic discharge patterns of bursting cold fibers related to hypothetical receptor mechanisms”, Pflügers Arch., 386(1) (1980) 1–9.

[12] Clewley, R. H., Sherwood, W. E., Lamar, M. D., Guckenheimer, J. M., “PyDSTool, a software environment for dynamical systems modeling, URL=http://pydstool.sourceforge.net”, (2007).

[13] Atherton, L. A., Prince, L. Y., Tsaneva-Atanasova, K., “Bifurcation analysis of a two-compartment hippocampal pyramidal cell model”, J Comput Neuroscience, 41 (2016) 91–106.

[14] Ananthkrishnan, N., Gupta, N. K., Sinha, N. K., “Computational Bifurcation Analysis of Multiparameter Dynamical Systems”, Journal of Guidance Control and Dynamics, 32(5) (2009) 1651-1653.

[15] Tsaneva-Atanasova, K., Osinga, H. M., Rieb, T., Sherman, A., “Full System Bifurcation Analysis of Endocrine Bursting Models”, J Theor Biol., 264(4) (2010) 1133–1146.

[16] Čupić, Z., Marković, V. M., Maćešić, S., Stanojević, A., Damjanović, S., Vukojević, V., Kolar-Anić, L., “Dynamic transitions in a model of the hypothalamic-pituitary-adrenal axis”, Chaos, 26(3) (2016) 033111.

[17] Takahashi, A., Kitajima H., Yazawa, T., “Bifurcation Analysis for Early Afterdepolarization in Shannon Model”, International Symposium on Nonlinear Theory and Its Applications, NOLTA2016, Yugawara, Japan, (2016).

[18] Tabak, J., Tomaiuolo, M., Gonzalez-Iglesias, A. E., Milescu, L. S., Bertram, R., “Fast activating voltage- and calcium-dependent potassium (BK) conductance promotes bursting in pituitary cells: a dynamic clamp study”, J Neurosci, 31(46) (2011) 16855–16863.

[19] Mrejeru, A., Wei, A., Ramirez, J. M., “Calcium-activated non-selective cation currents are involved in generation of tonic and bursting activity in dopamine neurons of the substantia nigra pars compacta”, J Physiol, 589(Pt 10): (2011) 2497–2514.

[20] Partridge, L. D., Müller, T. H., Swandulla, D., “Calcium-activated non-selective channels in the nervous system”, Brain Research Reviews, 19(3) (1994) 319-325.

[21] Sankaranarayanan, S., Simasko, S. M., "Potassium channel blockers have minimal effect on repolarization of spontaneous action potentials in rat pituitary lactotropes", Neuroendocrinology, 68 (1998) 297–311.
[22] Charles, A. C., Piros, E. T., Evans, C. J., Hales, T. G., "L-type Ca2+ channels and K+ channels specifically modulate the frequency and amplitude of spontaneous Ca2+ oscillations and have distinct roles in prolactin release in GH3 cells", J Biol Chem., 274(11) (1999) 7508–7515.
[23] Mei, Y. A., Soriani, O., Castel, H., Vaudry, H., Cazin, L., "Adenosine potentiates the delayed-rectifier potassium conductance but has no effect on the hyperpolarization-activated Ih current in frog melanotrophs", Brain Res, 793(1-2) (1998) 271–278.
[24] Song, Z., Xu, J., "Bursting near bautin bifurcation in a neural network with delay coupling", Int. J. Neur. Syst., 19(5) (2009) 359-373.
[25] Stojilkovic, S. S., "Pituitary cell type-specific electrical activity, calcium signaling and secretion", Biol Res., 39(3) (2006) 403-423.
[26] Jia, B., Gu, H., Li, L., Zhao, X., "Dynamics of period-doubling bifurcation to chaos in the spontaneous neural firing patterns", Cogn Neurodyn, 6(1) (2012) 89-106.
[27] Zemkova, H., Tomić, M., Kucka, M., Aguilera, G.,Stojilkovic, S.S., "Spontaneous and CRH-induced excitability and calcium signaling in mice corticotrophs involves sodium, calcium, and cation-conducting channels", Endocrinology, 157(4) (2016) 1576–1589.
[28] Shipston, M., "Control of anterior pituitary cell excitability by calcium-activated potassium channels", Mol Cell Endocrinol., 463 (2018) 37-48.

Current Address: Sevgi ŞENGÜL AYAN: Antalya Bilim University, Antalya TURKEY
E-mail Address: *sevgi.sengul@antalya.edu.tr*
ORCID: *https://orcid.org/0000-0003-0083-4446*

Current Address: Ahmet KURT: Antalya Bilim University, Antalya TURKEY
E-mail Address: *ahmet.kurt@std.antalya.edu.tr*
ORCID: *https://orcid.org/0000-0002-7175-1739*

INSTRUCTIONS TO CONTRIBUTORS

Communications Faculty of Sciences University of Ankara Series A2-A3: Physical Sciences and Engineering is a peer reviewed journal which has been published since 1948 by Ankara University, accepts original research articles written in English in the fields of Physics, Engineering Physics, Electronics/Computer Engineering, Astronomy and Geophysics. Review articles written by eminent scientists can also be invited by the Editor.

Manuscripts should be submitted as a single PDF file attached to an e-mail with a covering letter. In the covering letter, authors should nominate three potential reviewers and e-mailed the file to the most appropriate Area Editor of the research. The editorial office may not use these nominations, but this may help to speed up the selection of appropriate reviewers.

Manuscripts should be typeset using the LATEX typesetting system. Authors should prepare the article using the COMMUNICATIONS style before submission by e-mail. Manuscripts written in DOC form are also acceptable. A template of manuscript can be reviewed in **http://communications.science.ankara.edu.tr/index.php?series=A2A3&link=300**. After the acceptance of manuscripts for publication, we will ask you to submit the **TeX** form of the manuscript prepared in accordance with the style of the Journal. Authors are required to submit their Open Researcher and Contributor ID (**ORCID**) 's which can be obtained from http://orcid.org as their URL address in the format http://orcid.org/xxxx-xxxx-xxxx-xxxx. Acknowledgements should be given as short as possible at the end of the text. Formulas should be numbered consecutively in parentheses ( ). Footnotes should be avoided if possible, but when necessary, should be short and never contain any important part of the work and should be numbered consecutively by superscripts. All illustrations not including tables (photographs and other films, drawings, graphs, etc) must be labeled as "Figure". The proper position of each table and figure must be clearly indicated in the paper.

All tables and figures must have a number (Table 1, Figure 1) and a caption or legend. References including comments must be numbered consecutively in order of first appearance in the text. The reference number should be put in brackets [] where referred to in the text. References should be listed at the end of the manuscript in the numbered order in which they appear in the text as follows:

[1] Bairamov, E, Ozalp N., Uniform convergence and numerical computation of the Hubbell radiation rectangular source integral, *Radiation Physics and Chemistry*, 80 (2011) 1312–1315.
[2] Kelley, J. L., General Topology, Van Nostrand, 1970.

It is a fundamental condition that articles submitted to COMMUNICATIONS have not been previously published and will not be simultaneously submitted or published elsewhere. After the manuscript has been accepted for publication, the author will not be permitted to make any new additions to the manuscript.

Before publication, the galley proof is sent to the author for correction. Thus, it is solely the author's responsibility for any typographical mistakes occur in their article as it appears in the Journal. The contents of the manuscript published in the COMMUNICATIONS are the sole responsibility of the authors.

The PDF copies of accepted papers are free of charges, but hard copies of the paper, if required, are due to be charged for the amount of which is determined by the administration each year.

Commun. Fac. Sci. Univ. Ank. Ser. A2-A3.
Ankara University, Faculty of Sciences
06100, Besevler - ANKARA TURKEY
http://communications.science.ankara.edu.tr/index.php?series=A2A3

COMMUNICATIONS

DE LA FACULTE DES SCIENCES
DE L'UNIVERSITE D'ANKARA

FACULTY OF SCIENCES
ANKARA UNIVERSITY

VOLUME: 60 **Number: 1** **YEAR: 2018**

Series A2-A3: Physical Sciences and Engineering